

# Active and Passive Satellite Observations Coupled with Carbon–Nitrogen Synergy for Urban Fossil Fuel CO<sub>2</sub> Emissions Monitoring

Jinchun Yi <sup>#,1</sup>, Yiyang Huang <sup>#,1</sup>, Ge Han <sup>\*,1,3</sup>, Hongyuan Zhang <sup>2</sup>, Zhipeng Pei <sup>2</sup>, Haotian Luo <sup>1</sup>, Yichi Zhang <sup>1</sup>, Tianqi Shi <sup>6</sup>, Siwei Li <sup>1,3</sup>, Wei Gong <sup>4,5</sup>

<sup>1</sup>Hubei Key Laboratory of Quantitative Remote Sensing of Land and Atmosphere, School of Remote Sensing and Information Engineering, Wuhan University, Wuhan 430079, China.

<sup>2</sup>State Key Laboratory of Information Engineering in Surveying, Mapping and Remote Sensing, Wuhan University, Luoyu Road No.129, Wuhan 430079, China.

<sup>3</sup>Perception and Effectiveness Assessment for Carbon-neutrality Efforts, Engineering Research Center of Ministry of Education, Institute for Carbon Neutrality, Wuhan University, Wuhan, China.

<sup>4</sup>Electronic Information School, Wuhan University, Wuhan, China.

<sup>5</sup>Wuhan Institute of Quantum Technology, Wuhan, China.

<sup>6</sup>Laboratoire des Sciences du Climat et de l'Environnement, LSCE/IPSL, CEA-CNRS-UVSQ, Université Paris-Saclay, 91198 Gif-sur-Yvette, France.

*Correspondence to:* Ge Han (udhan@whu.edu.cn)

<sup>#</sup> These authors contributed equally to this work.

**Abstract.** Accurate estimation of fossil fuel CO<sub>2</sub> (ffCO<sub>2</sub>) emissions is essential for climate prediction and the development of mitigation policies. Top-down carbon – nitrogen joint observations offer the potential for more reliable ffCO<sub>2</sub> estimates. Here, we establish an inversion framework for urban ffCO<sub>2</sub> emissions based on combined active–passive satellite observations. Urban ffCO<sub>2</sub> distributions were first constructed using satellite NO<sub>2</sub> data and CO<sub>2</sub>-NO<sub>x</sub> emission ratios, and monthly ffCO<sub>2</sub> emissions for selected global cities were then estimated by integrating the total column dry-air carbon dioxide (XCO<sub>2</sub>) from the DQ-1 ACDL instrument. Our results show that satellite-derived NO<sub>x</sub> emissions provide strong constraints on urban anthropogenic CO<sub>2</sub> estimates. Validation against TCCON ground-based observations indicates that, compared with conventional top-down inversion approaches, our method more accurately reproduces urban ffXCO<sub>2</sub> plume distributions. We further evaluated the influence of different CO<sub>2</sub>-NO<sub>x</sub> ratio calculation methods on ffCO<sub>2</sub> estimates and found variations exceeding 150, exerting a substantial impact on emission inversions. Under observational constraints, the uncertainty in CO<sub>2</sub>-NO<sub>x</sub> ratios derived from different methods decreased by 9.79 – 38.78%, and the variation range was reduced by more than 100%, converging toward a consistent magnitude. This study advances understanding of the spatiotemporal patterns of urban ffCO<sub>2</sub> emissions and provides a unified perspective for future CO<sub>2</sub>-NO<sub>x</sub>-based anthropogenic carbon emission estimation.

## 1. Introduction

The intensification of global climate change has driven an increasing demand for high-precision monitoring of fossil fuel CO<sub>2</sub> (ffCO<sub>2</sub>) emissions (Agency, 2009). The Paris Agreement emphasizes that countries need rapid and timely access to changes in carbon emissions to support policy formulation and implementation. Achieving this goal relies on accurate and verifiable carbon accounting systems. Cities, due to their high concentration of population, energy consumption, and economic activity, contribute over 70% of global anthropogenic CO<sub>2</sub> emissions, making them key units for evaluating emission reduction policies and compliance monitoring (Crippa et al., 2018). Existing global and regional emission inventories primarily adopt bottom-up statistical accounting methods, estimating emissions based on energy production and sector-specific emission factors (Xu et al., 2024; Wei, 2024). However, these inventories often suffer from significant uncertainties due to data delays and incompleteness (Le Quéré et al., 2018).

To overcome the limitations of bottom-up approaches, top-down atmospheric inversion techniques have advanced rapidly in recent years, enabling constraints on regional carbon budgets. Passive satellite remote sensing systems, such as GOSAT and OCO-2/3, can invert XCO<sub>2</sub> over large portions of the globe and have unique potential for identifying local point sources, estimating regional carbon fluxes, and inferring gross primary productivity (Schwandner et al., 2017; Eldering et al., 2017; Sun et al., 2018b). Nonetheless, top-down inversion methods also rely on accurate prior emission estimates. Inventories that downscale national or regional emissions to high spatial and temporal resolution often suffer from incomplete socio-economic data and inaccurate emission conversion factors, leading to substantial uncertainties in urban emission estimates (Xing et al., 2025; Xu et al., 2025a). Moreover, conventional top-down CO<sub>2</sub> inversion studies have focused primarily on quantifying terrestrial ecosystem carbon fluxes, typically assuming fossil fuel emissions are known and unbiased (Pei et al., 2022). This complicates direct inference of anthropogenic emissions from CO<sub>2</sub> observations due to the atmospheric mixing of fossil fuel and ecosystem fluxes (Ye et al., 2020).

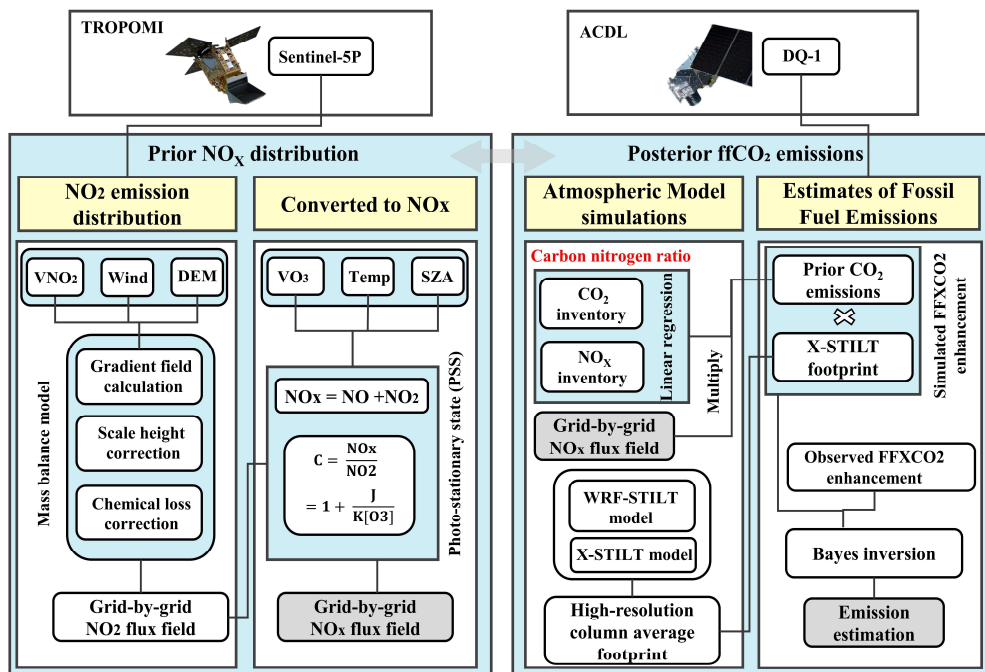
Coupled carbon-nitrogen observations offer a new perspective to address this gap (Reuter et al., 2019; Yang et al., 2023). Nitrogen oxides (NO<sub>x</sub> = NO + NO<sub>2</sub>) are major co-emitted species from fossil fuel combustion, with emission intensity and spatial distribution closely correlated with ffCO<sub>2</sub> (Feng et al., 2024). Studies have shown that in regions with varying pollution levels, XCO<sub>2</sub> anomalies spatially correlate with tropospheric NO<sub>2</sub> column densities (Hakkorainen et al., 2016). Moreover, the CO<sub>2</sub>-to-NO<sub>x</sub> ratio is often more stable than individual emission amounts because systematic biases in fossil fuel consumption affect both CO<sub>2</sub> and NO<sub>x</sub> statistics (Konovalov et al., 2016). Recent research suggests that optimized NO<sub>x</sub> emissions, combined with CO<sub>2</sub>-to-NO<sub>x</sub> ratios from bottom-up inventories, can provide more accurate ffCO<sub>2</sub> estimates (Zheng et al., 2020). For instance, Zheng et al. used TROPOMI NO<sub>2</sub> data to estimate 10-day moving averages of Chinese ffCO<sub>2</sub> emissions during the COVID-19 pandemic, finding an 11.5% decline compared to the same period in 2019 (Zheng et al., 2020). Liu et al. validated the feasibility of NO<sub>x</sub>-based ffCO<sub>2</sub> estimation by comparing inferred CO<sub>2</sub> emissions with highly accurate stack measurements from eight large US power plant (Liu et al., 2020). High-resolution NO<sub>2</sub> column observations, such as those from Sentinel-5P/TROPOMI, can be inverted using a mass-balance

60 framework to derive accurate  $\text{NO}_x$  gridded fluxes(Qin et al., 2023; Sun, 2022). These  $\text{NO}_x$  fluxes can inform the prior spatial  
61 allocation of  $\text{CO}_2$  emissions due to the co-emission consistency of fossil fuel sources, and the high temporal resolution of TROPOMI  
62 allows rapid updates of  $\text{CO}_2$  priors, mitigating the lag inherent in static inventories(Zhang et al., 2022).

63 The  $\text{CO}_2$ -to- $\text{NO}_x$  ratio is crucial for converting  $\text{NO}_x$  emissions into  $\text{ffCO}_2$  estimates. However, because the  $\text{CO}_2$ -to- $\text{NO}_x$  ratio  
64 used in this study is calculated from  $\text{CO}_2$  emissions and  $\text{NO}_x$  emissions, there is currently a lack of accurate top-down measurement  
65 methods, most studies derive this ratio from inventories, and different calculation methods yield significantly different values.  
66 Assimilating observational data to invert  $\text{CO}_2$ -to- $\text{NO}_x$  ratios is therefore key to reducing uncertainties in  $\text{ffCO}_2$  estimation. Passive  
67 top-down observations are limited by cloud cover, aerosols, and solar irradiance, and in complex multi-source and topographic  
68 environments, signal attribution is challenging, restricting the accuracy and stability of city-scale inversions(Miller et al., 2014; Han  
69 et al., 2026).

70 In 2022, China launched DQ-1, the world's first  $\text{CO}_2$  lidar satellite, equipped with an IPDA lidar (ACDL) capable of high  
71 signal-to-noise ratio, day-and-night, all-weather observations. The dual-wavelength differential method mitigates interference from  
72 aerosols and thin clouds(Han et al., 2025). Compared to passive satellites, IPDA lidar offers unique advantages in urban plume  
73 detection and fine-scale emission inversion(Kiemle et al., 2017; Zhang et al., 2026). Previous studies using DQ-1  $\text{XCO}_2$  data  
74 successfully constrained point-source emissions(Cheng et al., 2025; Han et al., 2024; Zhang et al., 2025), and Yi et al. developed a  
75 kilometer-scale urban flux inversion system based on ACDL measurements, comparing its constraints to passive systems like OCO-  
76 2/3(Yi et al., 2025).

77 In this study, we propose a city-scale  $\text{ffCO}_2$  inversion framework that jointly assimilates active and passive satellite observations,  
78 dynamically bridging  $\text{NO}_x$  and  $\text{CO}_2$  emissions via the  $\text{CO}_2$ -to- $\text{NO}_x$  ratio. The workflow is illustrated in Fig. 1. TROPOMI  $\text{NO}_2$   
79 column data are first used to invert  $\text{NO}_x$  gridded emissions via a mass-balance approach. Combined with prior  $\text{CO}_2$ -to- $\text{NO}_x$  ratios,  
80 these  $\text{NO}_x$  fluxes are converted into  $\text{CO}_2$  priors. DQ-1  $\text{XCO}_2$ -Lidar along-track measurements are then assimilated using WRF-  
81 STILT high-resolution atmospheric transport simulations within a Bayesian inversion framework to estimate total city emissions  
82 and explicitly quantify observational and transport uncertainties. We applied this approach to Beijing, Paris, and Cairo, representing  
83 cities with diverse topographies and emission patterns, using August 2022 TROPOMI and DQ-1/ACDL data to evaluate the  
84 framework's ability to provide robust, high-resolution urban emission estimates. It is noteworthy that no unified  $\text{CO}_2$ -to- $\text{NO}_x$  ratio  
85 calculation method currently exists, and different methods yield divergent values, which can significantly bias final emission  
86 estimates. This study systematically evaluates the influence of prior  $\text{CO}_2$ -to- $\text{NO}_x$  ratio calculation methods on inversion outcomes,  
87 demonstrating that Bayesian assimilation can substantially reduce this uncertainty, converging different ratios to a consistent  
88 magnitude. This framework offers a unified approach for estimating urban emissions under limited or uncertain inventory conditions,  
89 providing a timely and reliable method for reporting anthropogenic  $\text{CO}_2$  emissions at the city scale.



90  
91 **Figure 1** Technical framework diagram

92 The remainder of this paper is structured as follows. Section 2 introduces the datasets and methods used in this study. Section  
93 3 presents the results of NO<sub>x</sub> emission estimation in Paris, Cairo, and Beijing based on TROPOMI observations combined with a  
94 mass-balance approach, followed by city-scale ffCO<sub>2</sub> inversion results obtained by assimilating DQ-1 ACDL observations within a  
95 Bayesian framework. Section 4 examines the influence of different prior CO<sub>2</sub>-to-NO<sub>x</sub> ratio calculation methods on the inversion  
96 process and highlights the importance of optimizing the CO<sub>2</sub>-to-NO<sub>x</sub> ratio using observational data. Finally, Section 5 summarizes  
97 and discusses the potential of the multi-source satellite Bayesian inversion framework for constraining urban CO<sub>2</sub> emissions, and  
98 emphasizes the significance of optimized CO<sub>2</sub>-to-NO<sub>x</sub> ratios for improving the accuracy of urban ffCO<sub>2</sub> estimates.

99 **2. Materials and methods**

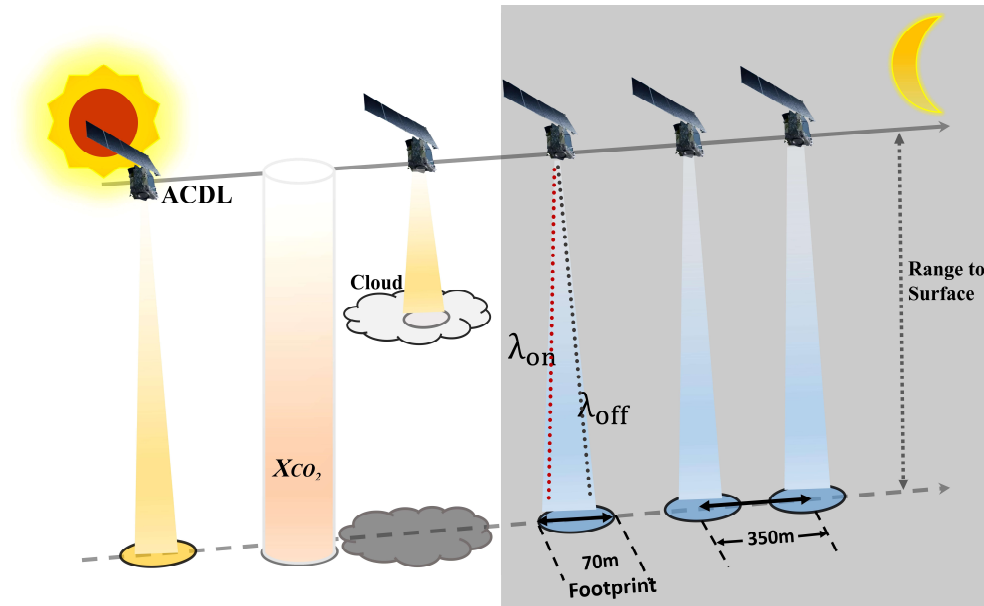
100 **2.1. Data**

101 **2.1.1. ACDL Productions**

102 The concept of DQ-1 was first proposed in 2012 with the aim of developing a satellite-borne lidar system analogous to the  
103 Cloud-Aerosol Lidar with Orthogonal Polarization (CALIOP) onboard CALIPSO, and it was officially approved as a national

104 project in 2017(Zhang et al., 2024). Unlike conventional environmental monitoring satellites, DQ-1 is distinguished by its  
105 breakthrough active remote sensing payload—the Atmospheric Carbon Dioxide Differential Absorption Lidar (ACDL)—which  
106 enables active “top-down” observations of atmospheric CO<sub>2</sub>(Zhang et al., 2023). The ACDL underwent successive stages of  
107 laboratory prototype development and airborne validation before its successful launch onboard the DQ-1 satellite into a near-polar  
108 sun-synchronous orbit at an altitude of ~705 km on April 18, 2022. Operational observations commenced in late May of the same  
109 year. This study primarily analyzes data collected August 2022.

110 The ACDL operates on the principle of Integrated Path Differential Absorption (IPDA) lidar, retrieving atmospheric column-  
111 averaged CO<sub>2</sub> concentrations (XCO<sub>2</sub>) via differential absorption techniques. The inversion methodology and data product  
112 specifications have been described in detail elsewhere; here, we provide only a brief overview(Han et al., 2025). The instrument  
113 transmits two nearly simultaneous laser pulses: one at a strong absorption line of CO<sub>2</sub> (R16, referred to as the “online” wavelength)  
114 and the other at a nearby weak absorption line (the “offline” wavelength). These are stabilized at 6361.225 cm<sup>-1</sup> and 6360.981 cm<sup>-1</sup>,  
115 corresponding to 1572.024 nm and 1572.085 nm, respectively. By comparing the differential attenuation between the online and  
116 offline signals, the system effectively mitigates the influence of aerosols and other interfering species, except water vapor, thereby  
117 enabling accurate retrievals of XCO<sub>2</sub>. The inversion process relies on dedicated algorithms, with the central concept being that the  
118 small wavelength offset produces differential absorption, which enhances the sensitivity of CO<sub>2</sub> detection (details of the ACDL  
119 XCO<sub>2</sub> retrieval algorithm are provided in the Appendix A1).



120  
121 **Figure 2 the schematic diagram for DQ-1's detection principle**

122  
123 Figure 2 illustrates the schematic of the DQ-1 measurement principle. The XCO<sub>2</sub> products generated by ACDL are provided in  
124 a point-sampling mode analogous to that of GOSAT. The lidar records one footprint of approximately 70 m every ~350 m along the  
125 satellite ground track. Additional details of the ACDL operating parameters are provided in the Appendix A1.

### 126 2.1.2. TROPOMI Productions

127 TROPOMI is a nadir-viewing spectrometer onboard ESA's Sentinel-5 Precursor (S5P) satellite, which was launched in October  
128 2017. Operating in an ascending Sun-synchronous polar orbit with an equator crossing time of approximately 13:30 local time,  
129 TROPOMI measures a range of trace gases as well as cloud and aerosol properties across four spectral channels (ultraviolet, visible,  
130 near-infrared, and shortwave infrared). The instrument's minimum pixel size was about  $3.5 \times 7$  km<sup>2</sup> at nadir before being reduced  
131 to  $\sim 3.5 \times 5.5$  km<sup>2</sup> on 6 August 2019 (Veeffkind et al., 2012). In this study, we used the SSP-PAL dataset (consistent with version  
132 2.3.1) (Eskes et al., 2021) covering the period from 1 August to 1 September 2022, obtained from <https://data-portal.s5p-pal.com>

133 To ensure data quality, we filtered out pixels with a `qa_value < 0.75` (Qin et al., 2023), and, following van Geffen et al., removed  
134 cloudy pixels (cloud radiance fraction > 50%) as well as anomalies (e.g., eclipses) from the TROPOMI NO<sub>2</sub> dataset (Van Geffen et  
135 al., 2022). To test our algorithm framework on a robust dataset, we selected summer NO<sub>2</sub> observations for three cities located in the  
136 mid-latitudes of the Northern Hemisphere, avoiding winter measurements that may be complicated by potential snow cover.  
137 Furthermore, given the need for city-scale accuracy, air mass factor (AMF) corrections were applied locally following the method  
138 described in (Beirle et al., 2023).

139 Sun et al. proposed an oversampling algorithm to project multi-satellite, multi-species observations onto a common grid, with  
140 code publicly available on GitHub ([https://github.com/Kang-Sun-CfA/Oversampling\\_matlab/](https://github.com/Kang-Sun-CfA/Oversampling_matlab/)) (Sun et al., 2018a). In this work, we  
141 applied this algorithm to the pre-processed TROPOMI overpass data, generating oversampled grids at 1 km resolution following  
142 the procedure described in (Sun, 2022).

### 143 2.1.3. Meteorological and DEM data

144 For the estimation of CO<sub>2</sub> emissions through model simulations, we utilized meteorological parameters from the National  
145 Centers for Environmental Prediction Final (NCEP FNL) operational global analysis dataset (National Centers for Environmental  
146 Prediction/National Weather Service/NOAA/U.S. Department of Commerce, 2015). The ds083.3 dataset is provided on a  $0.25^\circ \times$   
147  $0.25^\circ$  latitude-longitude grid and updated every six hours via the Global Data Assimilation System (GDAS)  
148 (<https://rda.ucar.edu/datasets/ds083-3/>). It covers 32 vertical levels, ranging from the surface to the top of the atmosphere, including  
149 the ground level and 31 isobaric layers from 1000 hPa to 1 hPa. Essential variables such as surface pressure, geopotential height,  
150 temperature, relative humidity, and zonal and meridional wind components were used as the main meteorological inputs for driving

151 the WRF-STILT simulations.

152 The wind vector data were obtained from the ERA5 reanalysis dataset (<https://doi.org/10.24381/cds.adbb2d47>)(Hersbach et  
153 al., 2023). We extracted hourly 10 m and 100 m wind vectors at 0.25° spatial resolution for the three selected cities during the period  
154 from 1 August to 1 September 2022. The 10 m wind vectors are used to approximate near-surface winds, whereas the 100 m wind  
155 vectors represent horizontal transport within the planetary boundary layer. These data were averaged to daily values and  
156 subsequently interpolated to match the grid resolution of the column concentration fields described in Section 2.3.1.

157 Digital elevation data were obtained from the GMTED2010 dataset (<https://www.usgs.gov/coastal-changes-and-impacts/gmted2010>)(Danielson and Gesch, 2011). The DEM was resampled and mapped to the same spatial grid as the  
158 concentration and wind fields to ensure consistency across all datasets.  
159

#### 160 **2.1.4. Emissions Inventory**

161 In this study, multiple emission inventories were used to estimate fossil fuel CO<sub>2</sub> (ffCO<sub>2</sub>) emissions and to calculate the CO<sub>2</sub>-  
162 to-NO<sub>x</sub> ratio. In the urban observation system simulation experiment (Section 3), the GEMS inventory (0.1° resolution) for NO<sub>x</sub> and  
163 CO<sub>2</sub> emissions(Huang et al., 2017) was used to derive the prior CO<sub>2</sub>-to-NO<sub>x</sub> ratio (available at: <https://gems.sustech.edu.cn/data>).  
164 For comparison, we also employed the gridded fossil fuel CO<sub>2</sub> emissions inventory from the Open - source Data Inventory for  
165 Atmospheric Carbon dioxide (ODIAC, Version 2024, 1 km resolution; <https://db.cger.nies.go.jp/dataset/ODIAC/>). In Section 4, we  
166 further utilized the sectoral and 0.1° gridded NO<sub>x</sub> and CO<sub>2</sub> inventories from the Emissions Database for Global Atmospheric  
167 Research (EDGAR; [https://edgar.jrc.ec.europa.eu/emissions\\_data\\_and\\_maps](https://edgar.jrc.ec.europa.eu/emissions_data_and_maps))(Crippa et al., 2018), as well as the sectoral NO<sub>x</sub> and  
168 CO<sub>2</sub> inventories from the Multi-resolution Emission Inventory model for Climate and air pollution research (MEIC;  
169 <http://meicmodel.org.cn/>)(Team, 2012). Using different approaches to calculate the CO<sub>2</sub>-to-NO<sub>x</sub> ratio, we quantified the variations  
170 arising from different inventory inputs and assessed their impact on emission inversions.

## 171 **2.2. Methodology**

### 172 **2.2.1. Calculation of Prior Distribution for CO<sub>2</sub> Emissions**

#### 173 **(1) Mass Balance Method**

174 In previous studies, numerous works have detailed the theoretical derivation for inferring gridded fluxes from column  
175 observations(Huang et al., 2024; Koene et al., 2024; Qin et al., 2023; Rey-Pommier et al., 2025; Sun, 2022). Such frameworks are  
176 generally based on solutions to the atmospheric continuity equation. Divergence-based approaches typically rely on several key  
177 assumptions: (1) exchanges above the planetary boundary layer (column top) and at the surface (column bottom) are neglected,  
178 effectively assuming two-dimensional diffusion; (2) horizontal turbulent transport is ignored at coarse grid resolutions; and (3) the

179 deposition term  $S$  is treated using a first-order chemical approximation. Starting from the unsteady, source-driven atmospheric  
 180 continuity equation, the gridded flux of a given species, such as  $\text{NO}_2$ , can be derived from satellite column observations, with the  
 181 resulting flux  $\langle E_{\text{NO}_2} \rangle$  expressed as in Equation 1.

$$\langle E_{\text{NO}_2} \rangle = \langle \vec{u} \cdot (\nabla V_{\text{NO}_2}) \rangle + \frac{\langle V_{\text{NO}_2} \vec{u}_10 \cdot (\nabla z_0) \rangle}{H} + \frac{\langle V_{\text{NO}_2} \rangle}{\tau} \quad (1)$$

183 The detailed derivation is provided in Appendix A2. To fully exploit the available data while accounting for observational  
 184 errors, spatial gradients were computed along the zonal, meridional, and both diagonal directions. Gradients were numerically  
 185 approximated using second-order central differences, multiplied by the corresponding decomposed wind vectors, and then averaged.  
 186 For boundary grid points, one-sided differences were applied. Although using gradients in multiple directions helps reduce  
 187 directional dependence, the finite-difference gradient operator can amplify high-frequency retrieval noise in the original  $\text{NO}_2$  column  
 188 field. Therefore, the divergence-derived  $\text{NO}_x$  fluxes should not be interpreted as purely deterministic grid-cell emissions. Instead,  
 189 they represent monthly aggregated estimates subject to retrieval noise, wind-field uncertainty, chemical-parameter uncertainty, and  
 190 possible structured errors introduced by gradient operations and gridding. We further evaluate this sensitivity in Appendix A5.

## 191 (2) Convert $\text{NO}_2$ to $\text{NO}_x$

192 Nitrogen oxides ( $\text{NO}_x = \text{NO} + \text{NO}_2$ ) do not exist independently in the troposphere, as  $\text{NO}$  and  $\text{NO}_2$  continuously interconvert,  
 193 while the total  $\text{NO}_x$  remains relatively stable. To convert between  $\text{NO}_2$  column densities and total  $\text{NO}_x$  columns, Sun et al. applied a  
 194 fixed coefficient of 1.32. In this study, we adopt a more rigorous approach to derive the conversion factor, as expressed in Equation  
 195 2(Beirle et al., 2023), based on the photostationary steady-state assumption:

$$\left\{ \begin{array}{l} V_{\text{NO}_x} = \alpha V_{\text{NO}} = \left( 1 + \frac{J}{K X_{\text{O}_3}} \right) V_{\text{NO}} \\ J = k_1 * \exp\left(-\frac{k_2}{\cos(\text{SZA})}\right) \\ K = k_3 * \exp\left(-\frac{k_4}{T}\right) \end{array} \right. \quad (2)$$

197 Here,  $J$  represents the photolysis frequency of  $\text{NO}_2$ , calculated following the methodology in (Dickerson et al., 1982). The rate  
 198 constants  $k_1$  and  $k_2$  are set to 0.0167 and 0.575, respectively. The solar zenith angle (SZA) can be directly determined from the  
 199 local latitude, longitude, and time; in this study, SZA values are obtained from the TROPOMI satellite metadata.  $K$  denotes the  
 200 chemical reaction rate constants for  $\text{NO}$  with  $\text{O}_3$ , expressed in  $\text{cm}^3/(\text{mol} \cdot \text{s})$  and recommended by IUPAC, with  $k_3=2.07 \cdot 10^{-12}$  and  
 201  $k_4=1400$ . The ozone mixing ratio,  $X_{\text{O}_3}$ , is derived from the ESCiMo project (Breninkmeijer and Cai, 2016), and  $T$  represents the  
 202 boundary-layer mean temperature obtained from ERA5 reanalysis data. Under these definitions, Equation 2 can be rewritten as:

$$X = \alpha * \langle E_{\text{NO}} \rangle \quad (3)$$

204 Using Equation 3 we can obtain grid-resolved estimates of  $\text{NO}_x$  fluxes, which serve as the prior distribution for fossil fuel  $\text{CO}_2$

205 (ffCO<sub>2</sub>) emissions. These estimates provide a data-driven prior inventory for subsequent steps in the inversion framework.

### 206 **(3) Scale height and Chemical lifetime**

207 Regarding the selection of scale height and first-order chemical lifetime, previous studies, such as Beirle et al., employed fixed  
208 empirical scale height values and adjusted terrain correction terms to obtain optimal estimates(Beirle et al., 2023). Their chemical  
209 lifetime was calculated using a compensation method that accounted for losses integrated over residence times within a 15 km buffer.  
210 While effective at point-source scales, this approach is not directly applicable to our study. In the present work, we follow Sun et  
211 al.'s purely data-driven approach, which leverages observational data without introducing additional assumptions, constructing a  
212 linear regression model to determine these parameters(Sun, 2022). This observation-driven fitting method not only reduces errors  
213 arising from new assumptions but also mitigates biases caused by grid resampling and near-surface wind selection.

214 To suppress excessive noise in single-day fits, we perform monthly regressions and adopt the temporal and spatial mean over  
215 the month as the final estimate, representing an aggregate over the full spatial domain, the entire month, and the troposphere. The  
216 retrieved scale height and first-order chemical lifetime are then applied back into Equations 4 and 6 to obtain the final gridded NO<sub>x</sub>  
217 vertical fluxes.

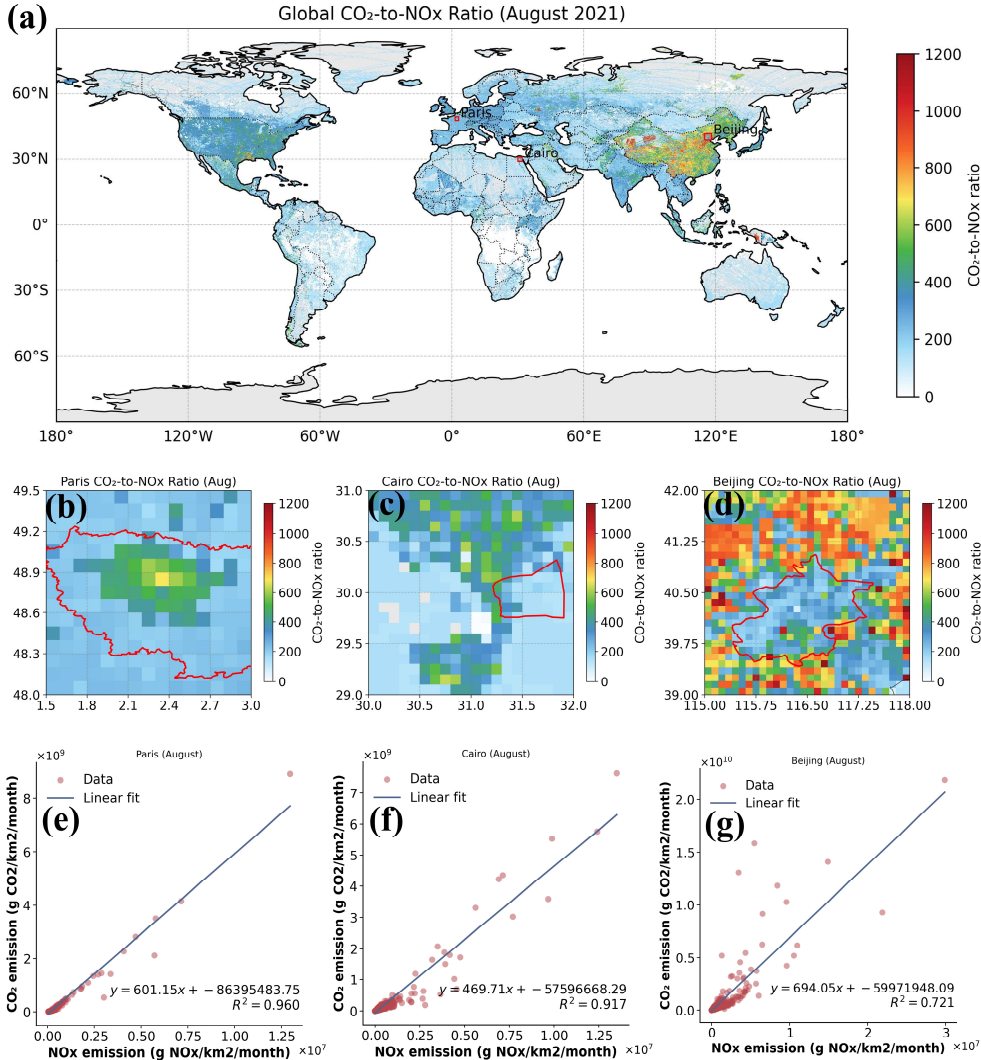
218 After terrain correction, the gridded flux fields remove a substantial portion of strong emission signals obscured by wind  
219 divergence and negative divergence artifacts, while the chemical correction term adjusts residual minor negative biases(Sun, 2022;  
220 Beirle et al., 2023). Any remaining small negative values after these corrections are set to zero.

### 221 **(4) Calculation of Prior CO<sub>2</sub>-to-NO<sub>x</sub> Ratio**

222 We used the prior CO<sub>2</sub>-to-NO<sub>x</sub> ratio in combination with TROPOMI-derived NO<sub>x</sub> emission distributions to obtain an initial  
223 characterization of urban prior ffCO<sub>2</sub> emissions. Following the approach of Feng et al., who calculated the CO<sub>2</sub>-to-NO<sub>x</sub> ratio by  
224 dividing gridded CO<sub>2</sub> and NO<sub>x</sub> emission inventories(Feng et al., 2024), we derived city-specific prior CO<sub>2</sub>-to-NO<sub>x</sub> ratio using the  
225 0.1° CO<sub>2</sub> and NO<sub>x</sub> inventories from GEMS (<https://gems.sustech.edu.cn/data/database>). Unlike Feng et al., who focused on grid-  
226 level CO<sub>2</sub>-to-NO<sub>x</sub> ratio, we fitted the gridded ratios across each study region to obtain an integrated city-level CO<sub>2</sub>-to-NO<sub>x</sub> ratio,  
227 which is more suitable for subsequent inversion analyses (Fig. 3). Details on the associated uncertainties are provided in Section  
228 4.1.

229 Figure 3 illustrates our method for calculating the prior CO<sub>2</sub>-to-NO<sub>x</sub> ratio. By fitting the 0.1° gridded ratios for each city, we  
230 obtained overall city-scale values. The coefficients of determination (R<sup>2</sup>) for Paris, Cairo, and Beijing were 0.96, 0.917, and 0.76,  
231 respectively.

232



233

234

235

236

237

238

239

240

Figure 3 Schematic diagram of prior CO<sub>2</sub>-to-NO<sub>x</sub> ratio calculation methods. Panel (a) shows the global gridded CO<sub>2</sub>-to-NO<sub>x</sub> ratio derived from GMES data. Panels (b)–(d) present the gridded CO<sub>2</sub>-to-NO<sub>x</sub> ratio for Paris, Cairo, and Beijing (the red lines indicate the boundaries of each city). Panels (e)–(g) display the overall CO<sub>2</sub>-to-NO<sub>x</sub> ratio fitting results for the three cities. We used the Île-de-France administrative boundary to depict Paris in the figures, rather than the city proper. Although our actual study area only covers a subset of Île-de-France (1.5–3° E, 48–49.5° N)

Recently, an increasing number of studies have employed NO<sub>x</sub> emissions to estimate ffCO<sub>2</sub> emissions (Feng et al., 2024; Zheng et al., 2020; Xu et al., 2025b; Yang et al., 2023; Zhang et al., 2022). In inversion methods based on NO<sub>x</sub> emissions, the choice of the

241 prior CO<sub>2</sub>-to-NO<sub>x</sub> ratio directly affects the emission estimates. Uncertainty in the prior ratio propagates to the estimated ffCO<sub>2</sub>  
242 emissions, influencing both their magnitude and spatial distribution. To evaluate this effect, we selected several widely used CO<sub>2</sub>-  
243 to-NO<sub>x</sub> ratio calculation methods and systematically assessed their associated uncertainties (results see Section 4.1 and Appendix  
244 A6).

245 - M.1 Grid-level CO<sub>2</sub>-to-NO<sub>x</sub> ratio derived directly from gridded CO<sub>2</sub> and NO<sub>x</sub> inventories(Feng et al., 2024). Since this study  
246 scales emissions to the city level, we further fitted the grid-level ratios to obtain city-integrated CO<sub>2</sub>-to-NO<sub>x</sub> ratios. M.1  
247 calculations were based on the GEMS gridded inventory.

248 - M.2 CO<sub>2</sub>-to-NO<sub>x</sub> ratios calculated using sectoral emission factors for CO<sub>2</sub> and NO<sub>x</sub>(Zheng et al., 2020). We derived city-scale  
249 ratios by aggregating across all sectors. M.2 used the GEMS [sectoral emission factors.sectoral inventory](#).

250 - M.3 CO<sub>2</sub>-to-NO<sub>x</sub> ratios derived from near-real-time satellite observations. Background-stable NO<sub>x</sub> plumes were used to  
251 constrain CO<sub>2</sub> plumes, and joint fitting of the two concentrations was performed using the cross-sectional flux method(Xu et  
252 al., 2025b; Reuter et al., 2019). The CO<sub>2</sub>-to-NO<sub>x</sub> ratio was obtained directly from the half-width at half-maximum. Following  
253 this approach, we used TROPOMI and OCO-2 observations to calculate city-scale ratios.

254 - M.4 Same as M.2, but the MEIC sectoral inventory was used for Beijing.

255 - M.5 Same as M.1, but calculations were based on the EDGAR gridded inventory.

256 - M.6 Same as M.2, but calculations were based on the EDGAR sectoral inventory.

## 257 2.2.2. Estimating ffCO<sub>2</sub> emissions by WRF-STILT simulations

### 258 (1) Quantifying ffXCO<sub>2</sub> enhancements

259 Distinguishing anthropogenic emission signals from the surrounding “clean” background in XCO<sub>2</sub> observations is a central  
260 challenge for constraining urban carbon emissions via satellite. Definitions of “background” vary across studies. In this work, we  
261 define the background as atmospheric XCO<sub>2</sub> that is unaffected by local emissions within the study region. Following the approach  
262 proposed by (Ye et al., 2020)in constraining urban emissions using OCO-2 observations, we adopt a baseline calculation strategy  
263 that incorporates latitudinal gradients.

264 In this framework, XCO<sub>2</sub> is decomposed into two components:  $XCO_{2,trend}$ , representing the regional-scale, non-local trend,  
265 and  $XCO_{2,local}$ , whose standard deviation  $\sigma_{local}$  characterizes local-scale variability. Samples satisfying  $XCO_2 < XCO_{2,trend} +$   
266  $0.5\sigma_{local}$  are selected as “background samples,” as they exhibit lower local spatial variability compared with data influenced by  
267 fossil fuel emissions. These background samples are then subjected to linear regression to derive the background baseline and  
268 characterize its spatial variation.

## (2) X-Stochastic Time-Inverted Lagrangian Transport model for ACDL productions

We employ the X-STILT V1 model to trace CO<sub>2</sub> concentration variations driven by prior emission information. X-STILT integrates satellite profile data and enables a comprehensive uncertainty assessment of urban XCO<sub>2</sub> enhancements on a per-observation basis (Wu et al., 2018). Originally developed to extract urban signals from passive OCO-2 XCO<sub>2</sub> observations, we have adapted the framework for use with the active CO<sub>2</sub> satellite DQ-1, with appropriate modifications. The relationship between XCO<sub>2</sub><sup>Lidar</sup> (DQ-1 XCO<sub>2</sub> observations) measurements and the CO<sub>2</sub> vertical profile, CO<sub>2</sub>(p), can be formulated as follows:

$$XCO_2^{Lidar} = \frac{\int_{p_{surface}}^{p_{toa}} CO_2(p) WF(p) dp}{\int_{p_{surface}}^{p_{toa}} WF(p) dp} = \sum_{n=1}^{toa} \frac{WF(p_n)}{IWF} \cdot CO_2(p_n) \quad (4)$$

Here,  $p_{toa}$  represents the pressure at the bottom height of the ACDL, and  $p_{surface}$  represents the pressure corresponding to the surface elevation at the laser footprint.  $WF$  and  $IWF$  denote the weighting function and the normalized weighting function of the ACDL, respectively. A detailed description is provided in Appendix A1.

We approximate the CO<sub>2</sub> concentration by summing the background concentration with the simulated ffCO<sub>2</sub> enhancement. Here, the simulated ffCO<sub>2</sub> enhancement,  $\Delta CO_2^{ffCO_2}(p) = \langle ffCO_2, foot(p) \rangle$ , is obtained by interpolating the modeled ffCO<sub>2</sub> fluxes along tracer-tagged footprints. Consequently, the relationship between the ffCO<sub>2</sub> fluxes and the simulated  $XCO_2^{Lidar}_{mod}$ , is established, yielding the modeled fossil fuel CO<sub>2</sub> enhancement  $XCO_2^{Lidar}_{ffCO_2, mod}$  along the lidar track:

$$XCO_2^{Lidar}_{ffCO_2, mod} = XCO_2^{Lidar}_{mod} - XCO_2^{Lidar}_{background} = \sum_{n=1}^{toa} \frac{WF(p_n)}{IWF} \cdot \langle emissions, foot(p_n) \rangle \quad (5)$$

$XCO_2^{Lidar}_{background}$  represents the background concentration along the selected DQ-1 orbit (see Section 2.2.2 (1)). The operator  $\langle, \rangle$  denotes an inner product,  $emissions$  is the prior emission flux, and  $foot(p_n)$  represents the modeled footprint at different vertical layers. Using the above formulation, the mathematical foundation for the inversion is established. By integrating footprints across multiple release heights, the equation can be further simplified. In this study, we define the ffXCO<sub>2</sub> enhancement simulated via the atmospheric transport model as:

$$XSTILT^{Lidar} = \sum_{n=1}^{toa} \frac{WF(p_n)}{IWF} \cdot foot(h_n) \quad (6)$$

$$XCO_2^{Lidar}_{ffCO_2, mod} = \langle XSTILT^{Lidar}, emissions \rangle \quad (7)$$

Here,  $XSTILT^{Lidar}$  is defined as the column-averaged footprint, corresponding to the column-averaged CO<sub>2</sub> concentration. The inner product of the column-averaged footprint and the prior emission flux yields the simulated XCO<sub>2</sub> enhancement.

## (3) Bayes inversion

We used the NO<sub>x</sub> emissions obtained previously as prior fluxes and, through the CO<sub>2</sub>-to-NO<sub>x</sub> ratio, established the relationship

295 between the prior emissions and the XCO<sub>2</sub> observed by DQ-1 (Equation 9). The XCO<sub>2</sub> enhancements estimated from DQ-1  
 296 observations were then employed to impose “top-down” constraints on the simulated results. Following the approaches of (Che et  
 297 al., 2024; Ye et al., 2020; Sheng et al., 2025), we applied a Bayesian inversion framework to optimize the prior emission estimates.

$$298 \quad y_{obs} = y_{sim} \cdot \lambda + \varepsilon_p \quad (8)$$

299 Here,  $y_{obs}$  and  $y_{sim}$  represent the observed ffXCO<sub>2</sub> enhancements and the simulated NO<sub>x</sub> enhancements, respectively. The  
 300 symbol  $\lambda$  denotes the CO<sub>2</sub>-to-NO<sub>x</sub> ratio, and  $\varepsilon_p$  represents the observational error, which encompasses contributions from DQ-1  
 301 measurement uncertainties, model errors, and errors in model parameters. It is defined as follows:

$$302 \quad \begin{cases} y_{obs} = \int_{latitude1}^{latitude2} ffXCO2_{obs} dt \\ y_{sim} = \int_{latitude}^{latitude2} < X, footprint > dt \end{cases} \quad (9)$$

$$303 \quad \varepsilon_{obs} = \sqrt{\sigma_{measurement}^2 + \sigma_{sim}^2} \quad (10)$$

304 In this context, ffXCO<sub>2,obs</sub> represents the DQ-1 XCO<sub>2</sub> enhancement after background concentration removal. The notation  $<$   
 305  $X, footprint >$  denotes the simulated NO<sub>x</sub> enhancement, obtained by convolving the NO<sub>x</sub> emission inventory  $X$  with the STILT-  
 306 derived footprint (It should be noted that the footprints used here represent hourly footprints during the simulation period, whereas  
 307 the NO<sub>x</sub> emissions are monthly emissions derived using the method described in Section 2.2.1. Therefore, we use the New High  
 308 Resolution Temporal Profiles in EDGAR dataset ([https://edgar.jrc.ec.europa.eu/dataset\\_temp\\_profile](https://edgar.jrc.ec.europa.eu/dataset_temp_profile)) to distribute the monthly NO<sub>x</sub>  
 309 emissions to each hourly footprint). Pseudo-observations, ffXCO<sub>2,obs</sub>, are generated by averaging DQ-1 measurements over one-  
 310 second intervals along the satellite track (~7 km), together with the corresponding simulated values.

311 Following the Bayesian inversion approach, the state vector  $\lambda$  is expressed in terms of the CO<sub>2</sub>-to-NO<sub>x</sub> ratio, representing the  
 312 relationship between urban fossil fuel CO<sub>2</sub> and NO<sub>x</sub> emissions. The Jacobian matrix is derived from the simulated NO<sub>x</sub> enhancement  
 313  $y_{sim}$ . Here,  $\sigma_{measurement}^2$  represents the observational error variance, and  $\sigma_{sim}^2$  denotes the model transport error variance. DQ-1  
 314 observations are assumed unbiased with respect to the true state. To account for measurement uncertainty, random Gaussian noise  
 315 with a standard deviation of 0.3 ppm—representing the lower limit of observational error—is added to the observations.

316 By minimizing the loss function, we obtain the posterior CO<sub>2</sub>-to-NO<sub>x</sub> ratio  $\hat{\lambda}$  and posterior uncertainty  $\hat{\sigma}$  :

$$317 \quad \hat{\lambda} = \lambda + \sigma_{sim}^2 y_{sim}^T (y_{sim} S_{obs} y_{sim}^T + S_{obs})^{-1} (y_{obs} - y_{sim} \lambda) \quad (11)$$

$$318 \quad \hat{\sigma}^2 = (y_{sim}^T S_{obs}^{-1} y_{sim} + \sigma_{sim}^{-2})^{-1} \quad (12)$$

319 Here,  $S_{obs}$  is a diagonal matrix, with the diagonal entries representing the observational error variances  $\varepsilon_{obs}^2$  for each orbit.  
 320 the prior uncertainty  $\sigma_{sim}$  is primarily derived from the uncertainties in the prior NO<sub>x</sub> emission distribution  $\sigma_{NOx}$  and the prior

CO<sub>2</sub>-to-NO<sub>x</sub> ratio  $\sigma_{C/N}$  as equation 13:

$$\sigma_{sim} = \sqrt{\sigma_{NOx}^2 + \sigma_{C/N}^2} \quad (13)$$

### 3. Urban Observation System Simulation Experiment

#### 3.1. Satellite-driven urban NO<sub>x</sub> emission distribution

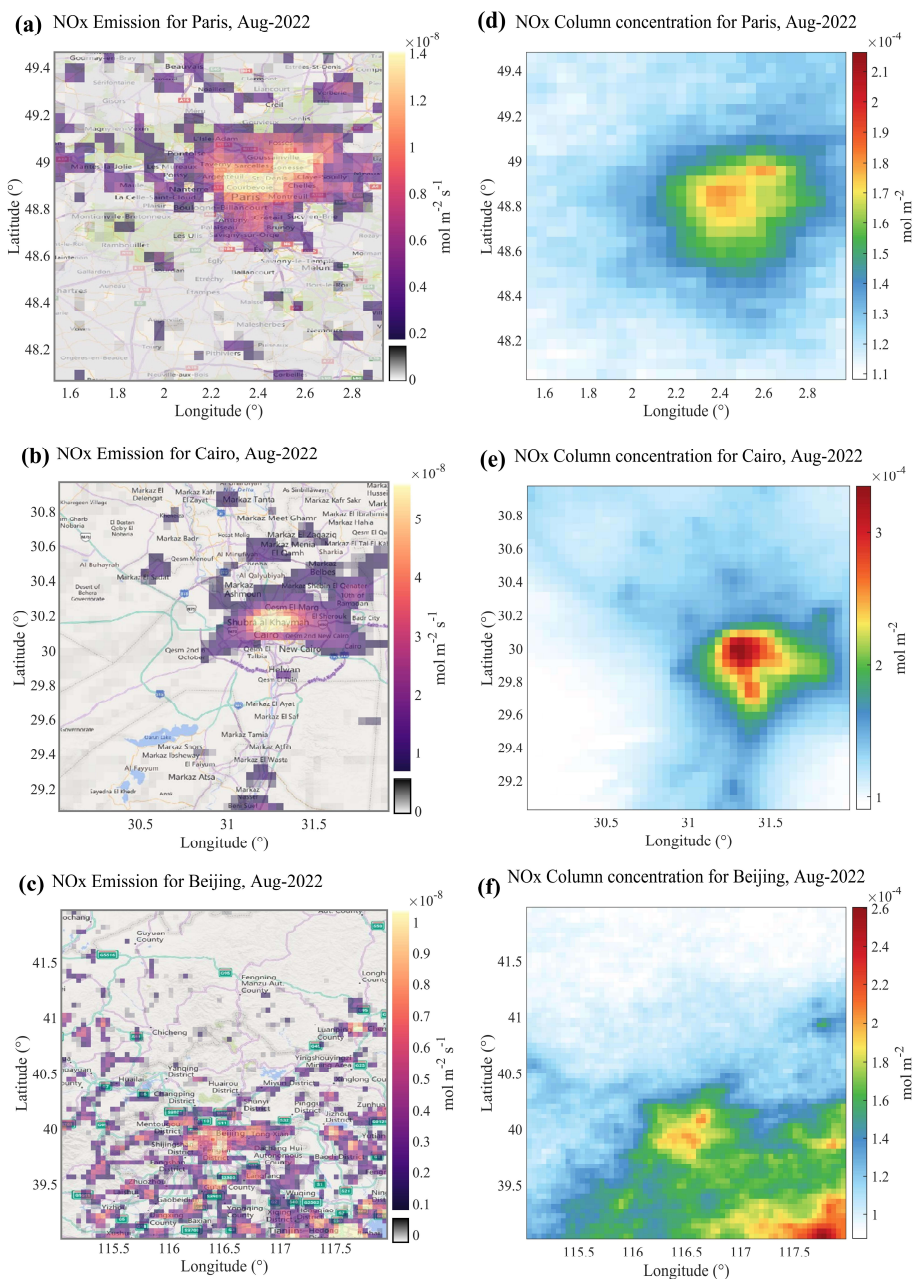
As described in Section 2.2.1, we applied the mass balance approach in the three cities to derive prior NO<sub>x</sub> gridded inventories, which serve as the basis for constructing ffCO<sub>2</sub> gridded emissions. The grid resolution was set to 5 km × 5 km. Figure 4 illustrates the detailed NO<sub>x</sub> fluxes for August 2022 over Beijing, Paris, and Cairo, produced entirely via a top-down approach, with panels (a)–(c) corresponding to Beijing, Paris, and Cairo, respectively.

From the figure, it is evident that the average NO<sub>x</sub> flux magnitude in all three cities is on the order of ~10<sup>-8</sup> mol m<sup>-2</sup> s<sup>-1</sup>. However, their spatial distributions differ considerably. Both Paris and Cairo exhibit highly concentrated emission patterns. In Cairo, the central urban area and industrial zones display peak NO<sub>x</sub> fluxes on the order of ~10<sup>-7</sup> mol m<sup>-2</sup> s<sup>-1</sup>. These high-flux regions sharply decrease with distance from the center, highlighting a pronounced urban boundary effect (Li et al., 2025). In contrast, Beijing not only exhibits strong emissions in the central urban area (within the Sixth Ring Road) but also features numerous dispersed point- and area-like sources in suburban districts (e.g., Fangshan in the southwest) and in the surrounding hills and mountains. Compared with Cairo's concentrated emissions, Beijing's peak NO<sub>x</sub> grid flux in the urban core is nearly one order of magnitude lower (see the color scale mapping in Fig. 4); however, due to the city's larger spatial extent, the total flux remains substantially higher than that of Cairo.

Beijing's topography, with higher elevations in the northwest and lower elevations in the southeast, can induce local wind divergence over hilly and mountainous areas. This effect may generate false positives when using the divergence method (Sun et al., 2021; Liu et al., 2021). In the northwestern suburban mountains of Beijing, the mean wind divergence can reach magnitudes of ~ ±10<sup>-4</sup> s<sup>-1</sup>, while TROPOMI NO<sub>2</sub> column densities are on the order of 10<sup>-4</sup> mol m<sup>-2</sup>. Such magnitudes are comparable to mid-scale urban averages or point-source emissions. Neglecting the divergence term can result in genuine emissions being omitted, while background fluxes induced by terrain or wind divergence are mistakenly included. Following (Sun, 2022), we applied Eq. A5 to reconstruct the wind-divergence term using surface wind and terrain gradients, thereby reintegrating previously neglected area-like emissions. Using Beirle et al.'s methodology, we integrated the net gridded fluxes within a 60 km radius centered on Beijing over the entire year of 2022 to estimate the city's annual NO<sub>x</sub> emissions at 251,450 t. This value is approximately 9.7% higher than the 2022 annual emission reported in the MEIC inventory for Beijing (227,000 t). Although the total magnitude is consistent, the spatial distribution from top-down estimates differs substantially from bottom-up inventories. Section 3.2.2 further analyzes these

349 differences by simulating urban ffCO<sub>2</sub> plumes using both our ffCO<sub>2</sub> inventory and the ODIAC inventory.

350 By comparison, Paris and Cairo are situated on relatively flat terrain (maximum elevation ~180 m). Terrain-induced wind  
351 divergence is negligible relative to total fluxes (wind-terrain and divergence contributions  $\sim 10^{-10}$  mol m<sup>-2</sup> s<sup>-1</sup>), leaving the continuity  
352 equation primarily governed by wind-weighted column gradients. Cairo, located upstream of the Nile Delta in a high-albedo desert  
353 region, benefits from low uncertainty in satellite-derived NO<sub>2</sub> columns. Under these conditions, the top-down NO<sub>x</sub> inventory closely  
354 aligns with the bottom-up inventory in terms of spatial distribution. Paris, situated in the Paris Basin along the Seine River,  
355 experiences minimal terrain gradients. Although less extreme than Cairo, the slight topographic variation still produces pronounced  
356 urban boundary effects in the inversion results.



357

358

359

Figure 4 Gridded prior NO<sub>x</sub> emission inventories derived from the mass balance method. Panels (a)–(c) show the NO<sub>x</sub> flux distributions (unit: mol/m<sup>2</sup>/s) for Beijing, Paris, and Cairo in August 2022. Panels (d)–(f) present the resampled monthly mean NO<sub>x</sub> column

360 concentration distributions for the three cities. Basemap for panels (a)–(c): Esri World Topographic Map. Sources: Esri, HERE, Garmin,  
361 Intermap, INCREMENT P, GEBCO, USGS, FAO, NPS, NRCan, GeoBase, IGN, Kadaster NL, Ordnance Survey, Esri Japan, METI,  
362 Mapwithyou, NOSTRA, © OpenStreetMap contributors, and the GIS user community.

363

364 To quantitatively compare the NO<sub>x</sub> emission characteristics and atmospheric behavior among Beijing, Paris, and Cairo, derived  
365 using the mass balance approach, we analyzed key parameters for August, including mean NO<sub>x</sub> fluxes, total emissions, chemical  
366 lifetimes, vertical distribution scale heights, and NO<sub>x</sub>/NO<sub>2</sub> ratios (Table 1). These NO<sub>x</sub> behavior parameters reflect heterogeneous  
367 characteristics shaped by the interplay of emission intensity, photochemical conditions, and boundary layer structure.

368 In terms of mean NO<sub>x</sub> flux per unit area (mol m<sup>-2</sup> s<sup>-1</sup>), Cairo exhibits the highest value (0.35 × 10<sup>-8</sup>), followed by Paris (0.28 ×  
369 10<sup>-8</sup>) and Beijing (0.24 × 10<sup>-8</sup>), indicating a higher emission of urban emission sources in Cairo—particularly from traffic—resulting  
370 in stronger NO<sub>x</sub> release per unit surface area. Nevertheless, Beijing’s total NO<sub>x</sub> emissions (182,800 t yr<sup>-1</sup>) are substantially higher  
371 than those of the other two cities, reflecting its larger urban extent and greater overall emission intensity, characteristic of a complex  
372 multi-source emission profile.

373 The first-order chemical lifetime of NO<sub>x</sub> in the atmosphere indicates its removal rate and is influenced by factors such as OH  
374 radical concentration and solar radiation intensity. Paris exhibits the longest NO<sub>x</sub> chemical lifetime (6.91 h), followed by Beijing  
375 (4.70 h) and Cairo (2.93 h). These differences are closely linked to photochemical activity: strong summer sunlight and high  
376 temperatures in Cairo enhance OH-driven removal reactions, whereas the relatively mild mid-latitude climate of Paris, combined  
377 with emission control measures, prolongs NO<sub>x</sub> lifetime.

378 Regarding vertical distribution, the NO<sub>x</sub> scale height also varies across the three cities. Beijing shows the highest scale height  
379 (2.08 km), reflecting the combined effects of strong convective transport and multi-source emissions that elevate NO<sub>x</sub> into the upper  
380 mixing layer. By contrast, Cairo (1.41 km) and Paris (1.21 km) display more typical boundary-layer-constrained distributions,  
381 indicating that ground-level emission controls and thermal structure strongly modulate vertical NO<sub>x</sub> transport.

382 Finally, the NO<sub>x</sub>/NO<sub>2</sub> ratio provides insight into the proportion of NO and its degree of conversion. Beijing exhibits the highest  
383 ratio (1.41), followed by Cairo (1.32) and Paris (1.29), suggesting a higher fraction of NO in Beijing, likely associated with dense  
384 traffic sources and a larger fraction of primary NO emissions. The relatively lower ratio in Paris reflects a higher NO<sub>2</sub> fraction,  
385 consistent with effective emission controls and extensive photochemical conversion.

386

387 **Table 1 Grid-averaged NO<sub>x</sub> fluxes, with total urban NO<sub>x</sub> emissions as intermediate parameters in the mass balance method.**

City	NO <sub>x</sub> average flux mol/(m <sup>2</sup> * s)	NO <sub>x</sub> total emission kt/month	Chemical lifetime(hour)	Scale height(km)	NO <sub>x</sub> /NO <sub>2</sub>
Beijing	0.235 10 <sup>^(-8)</sup>	15.29	4.69	2.07	1.41

Paris	$0.277 \cdot 10^{-8}$	4.45	6.90	1.21	1.29
Cairo	$0.353 \cdot 10^{-8}$	6.78	2.93	1.40	1.32

Details of the uncertainties are provided in the Appendix A5.

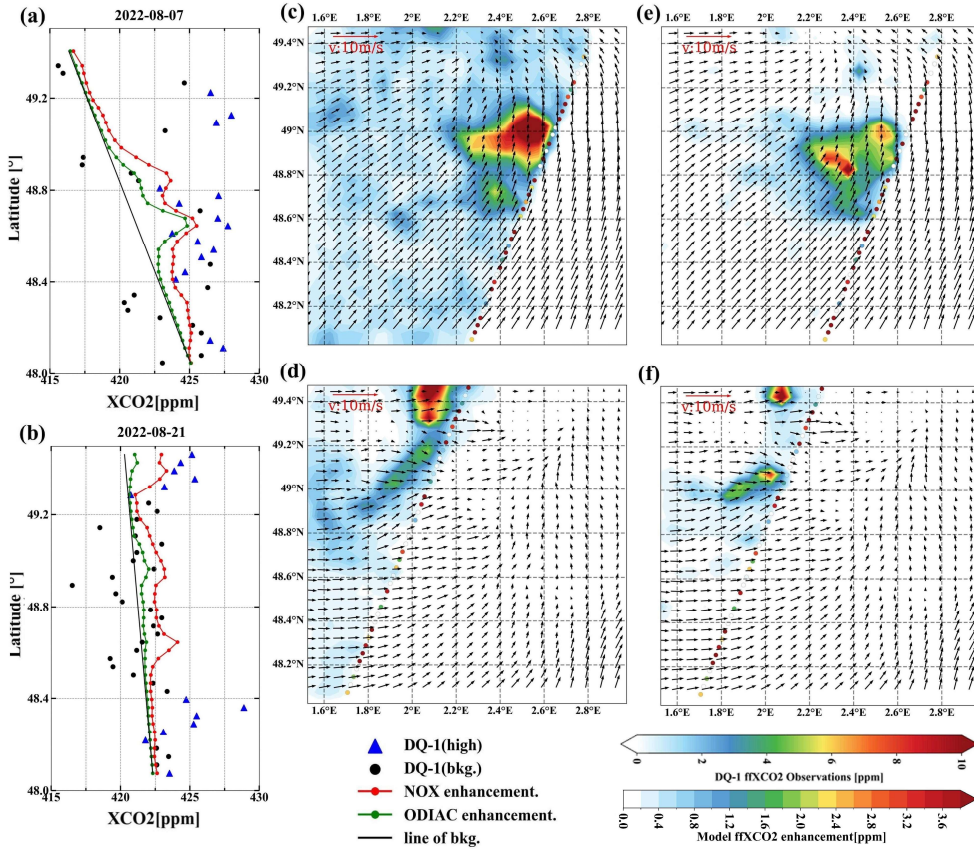
### 3.2. Urban Fossil Fuel XCO<sub>2</sub> Enhancement (ffXCO<sub>2</sub>)

In this section, we summarize the prior ffXCO<sub>2</sub> emissions for each study region. For the selected orbits, the total monthly emissions of Beijing, Paris, and Cairo were approximately 7.47–9.94, 2.91–3.33, and 2.73–3.60 MtC/month, respectively. To constrain emissions, we compared observed and simulated ffXCO<sub>2</sub> enhancements, where ffXCO<sub>2</sub> enhancement is defined as the increase in XCO<sub>2</sub> relative to the background level caused by local fossil fuel emissions. The prior ffXCO<sub>2</sub> enhancements were simulated by taking the inner product of prior NO<sub>x</sub> emissions inventories with STILT footprints, while the observed enhancements from DQ-1 were derived by subtracting the background concentration from the measured XCO<sub>2</sub>. By comparing prior and observed ffXCO<sub>2</sub> enhancements, we assessed the variability of ffXCO<sub>2</sub> along the orbit and investigated the sources and detectability of the ffXCO<sub>2</sub> signal.

#### 3.2.1. Comparison of Modeled and Observed ffXCO<sub>2</sub>

Complex horizontal wind fields can lead to elongated and non-Gaussian plume structures in simulated ffXCO<sub>2</sub> distributions (Ye et al., 2020). This feature is illustrated in Fig. 5c–f. Figures 5a and 5b show the simulated and observed XCO<sub>2</sub> along two overpasses (simulated XCO<sub>2</sub> is obtained by adding the simulated ffXCO<sub>2</sub> to the background derived in Section 2.2.2 (1)). Along these overpasses, ffXCO<sub>2</sub> enhancements exceeding 5 and 10 ppm were observed, with the measured enhancements consistently larger than the simulated values. Although the simulated peak on 7 August is narrower than the observed peak, and the observed peak near 48.4° on 21 August shows a ~0.3° displacement relative to the simulation, the overall magnitude of simulated ffXCO<sub>2</sub> agrees well with observations.

To further evaluate the feasibility of constraining fossil fuel CO<sub>2</sub> emissions using the NO<sub>x</sub> inventory, we performed a comparative analysis using the ODIAC inventory. We compared simulated ffXCO<sub>2</sub> during the satellite overpasses based on the NO<sub>x</sub> and ODIAC inventories (colored shaded areas in the figure), as well as their contributions to the pseudo-observed XCO<sub>2</sub> at the satellite locations (colored dots), where the red line represents enhancements derived from the NO<sub>x</sub> inventory and the green line represents those from ODIAC. Over Paris, the NO<sub>x</sub>-based simulation yields higher ffXCO<sub>2</sub> enhancements than ODIAC, likely due to uncertainty in the prior CO<sub>2</sub>-to-NO<sub>x</sub> ratio. Nonetheless, both inventories capture enhancements exceeding 4 ppm. Moreover, the line plots indicate that the temporal variation and magnitude of the simulated concentration contributions (red and green lines) are nearly identical.

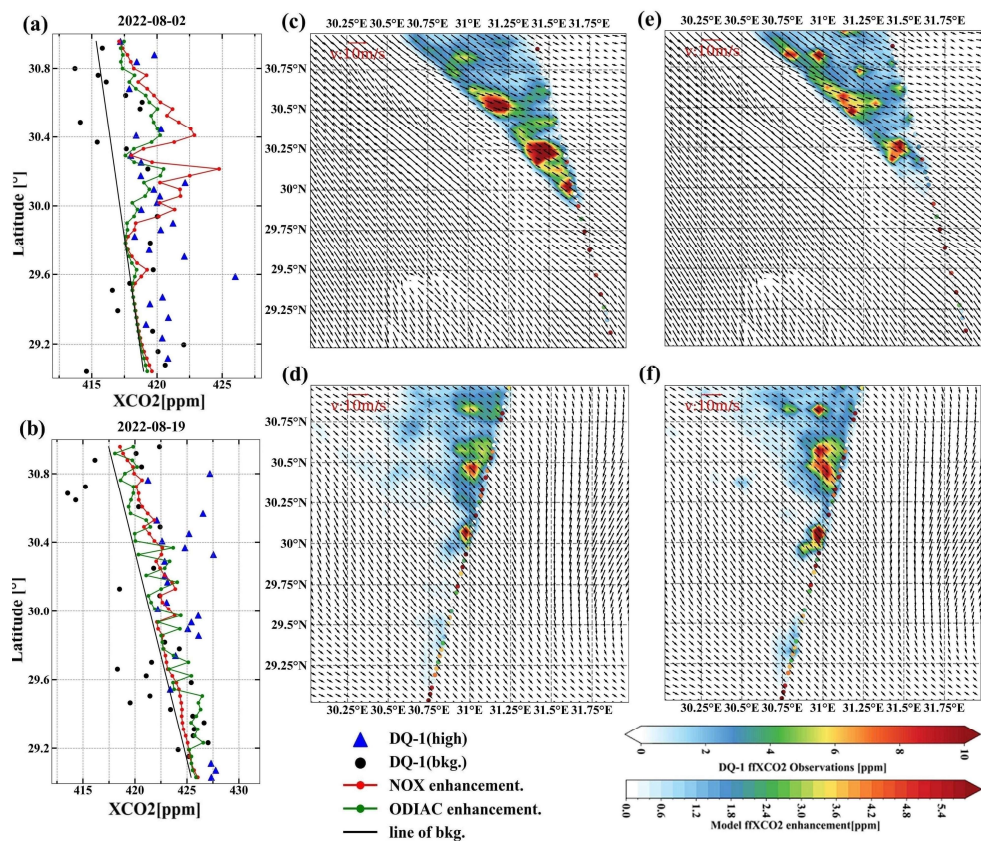


414  
 415 **Figure 5** Comparison between simulated and observed fFXCO<sub>2</sub> enhancements using DQ-1 overpasses above Paris on 7 August 2022 and  
 416 21 August 2022 at 01:00 UTC. Panels (a) and (b) show DQ-1 XCO<sub>2</sub> along the two tracks (black dots and blue triangles) and simulated  
 417 XCO<sub>2</sub> (red solid line: sum of background concentration and fFXCO<sub>2</sub> simulated using the NO<sub>x</sub> emissions; green solid line: sum of  
 418 background concentration and fFXCO<sub>2</sub> simulated using the ODIAC inventory), averaged over 0.5 s. Black circles denote the data used to  
 419 derive the background concentration (black solid line). Panels (c)–(f) show simulated fFXCO<sub>2</sub> and observed fFXCO<sub>2</sub> retrieved from DQ-1  
 420 data ((c), (d): based on the NO<sub>x</sub> inventory; (e), (f): based on the ODIAC inventory). Background XCO<sub>2</sub> concentrations have been subtracted.  
 421 The reference vector indicates a wind speed of 10 m/s.

422  
 423 We examined local fFXCO<sub>2</sub> enhancements during two overpasses of Cairo on 2 August 2022 at 11:00 and 19 August 2022 at  
 424 23:00. As shown in Fig. 6, the simulated fFXCO<sub>2</sub> peaks exceed 6 ppm. In contrast to Paris, where enhancements are widespread,  
 425 diffuse, and lack clear structure, and Beijing, where plumes exhibit complex patterns, the simulated fFXCO<sub>2</sub> over Cairo is strongly  
 426 influenced by northwesterly winds, resulting in well-defined plumes. Figure 5a illustrates that the simulations based on both  
 427 inventories on 2 August produce similar magnitudes and trends, consistent with the Paris results, where the NO<sub>x</sub>-based simulation

428 exceeds that from ODIAC. Notably, the simulated peaks on 2 August also show a spatial offset relative to the observations.  
 429 Following Ye et al. 2020, such offsets are attributed to the satellite trajectory crossing the plume edges nearly parallel to the plume  
 430 axis, making the simulated fXCO<sub>2</sub> highly sensitive to errors in the horizontal wind field.

431 Notably, the overpasses above Paris and Cairo (Figs. 5a and 6b) exhibit higher latitudinal gradients in the background XCO<sub>2</sub>,  
 432 as indicated by the background lines. The approach used to derive these background lines provides a reliable estimate of background  
 433 XCO<sub>2</sub> because, within the relevant regions, the observed and modeled cumulative fXCO<sub>2</sub> enhancements along the satellite track  
 434 are largely consistent. Consequently, these findings highlight the effectiveness of the background line method for inferring satellite-  
 435 observed background XCO<sub>2</sub>. They also emphasize that the spatial scale of satellite data analysis is closely linked to the constraints  
 436 imposed by local emission sources. Neglecting the latitudinal gradient of background XCO<sub>2</sub> may introduce biases in the estimation  
 437 of fXCO<sub>2</sub> and, consequently, in derived emission fluxes (Ye et al., 2020).

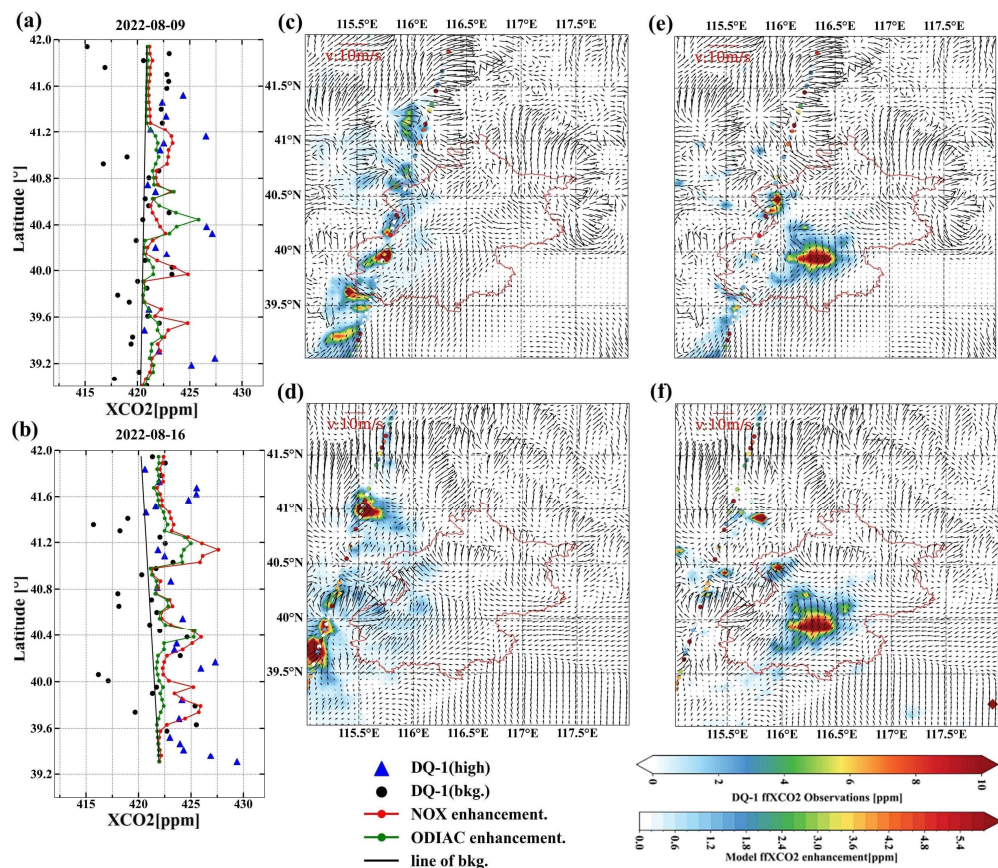


438  
 439 **Figure 6** Similar to Fig. 5, comparison between simulated and observed fXCO<sub>2</sub> enhancements using DQ-1 overpasses above Cairo on 2  
 440 August 2022 at 11:00 UTC (panels a, c, e) and 19 August 2022 at 23:00 UTC (panels b, d, f). Panels (c) and (d) show the simulated fXCO<sub>2</sub>

441 enhancements based on the NO<sub>x</sub> emissions, while panels (e) and (f) show those based on the ODIAC inventory.

442

443 3.2.2. Comparison of NO<sub>x</sub> and ODIAC Modeled fXCO<sub>2</sub> in Beijing



444

445 Figure 7 Similar to Fig. 5, comparison between simulated and observed fXCO<sub>2</sub> enhancements using DQ-1 overpasses above Beijing on 9  
446 August 2022 at 18:00 UTC (panels a, c, e) and 16 August 2022 at 18:00 UTC (panels b, d, f). Panels (c) and (d) show the simulated fXCO<sub>2</sub>  
447 enhancements based on the NO<sub>x</sub> emissions, while panels (e) and (f) show those based on the ODIAC inventory.

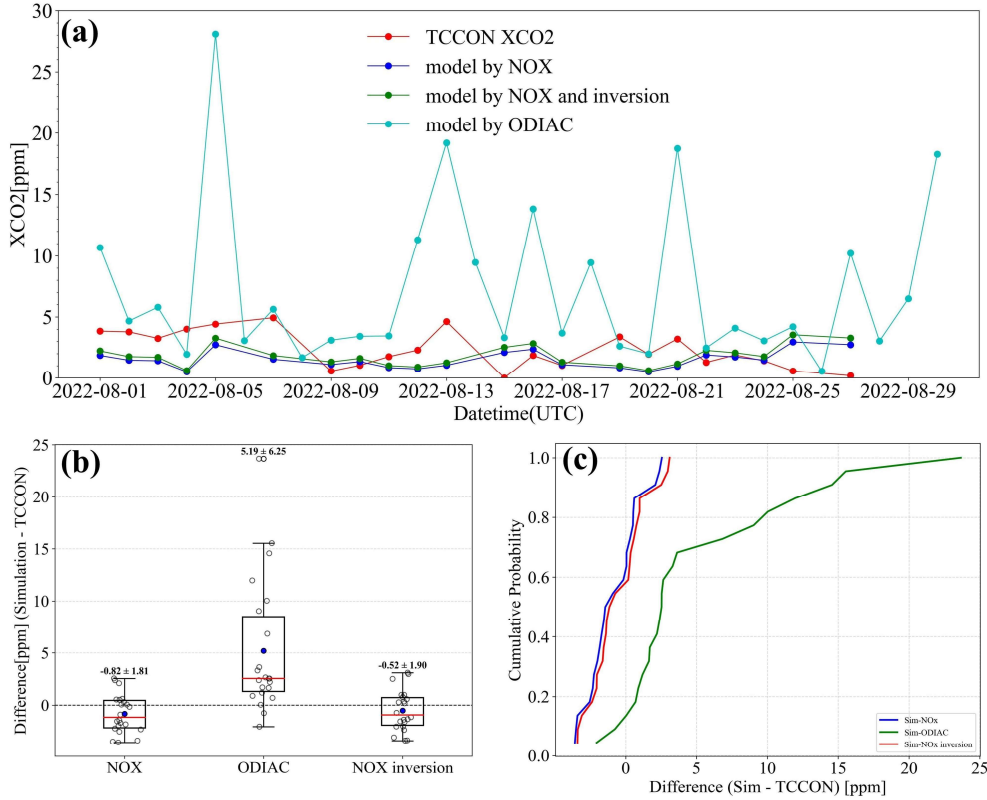
448

449 Figure 7 illustrates the investigation of local fXCO<sub>2</sub> enhancements over Beijing using two DQ-1 overpasses and corresponding  
450 simulated fXCO<sub>2</sub>. In the figure, the colored shading represents XCO<sub>2</sub> concentrations accumulated over the previous 24 hours  
451 simulated by STILT, while the colored dots indicate satellite-observed XCO<sub>2</sub> enhancements, calculated by subtracting the

452 background values (see Section 2.2.2). The red contours outline the urban area of Beijing. As shown, fXCO<sub>2</sub> over this region can  
453 reach approximately 6.0 ppm.

454 Notably, simulations based on the NO<sub>x</sub> inventory (Figs. 7c, d) show that the spatial distribution of fXCO<sub>2</sub> enhancements varies  
455 significantly with meteorological conditions and emission patterns. In contrast, for Paris and Cairo, the simulated fXCO<sub>2</sub> is more  
456 concentrated. Over Beijing, however, the fXCO<sub>2</sub> distribution is more dispersed and comprises multiple plumes. When comparing  
457 simulations using NO<sub>x</sub> and ODIAC inventories for Paris and Cairo, the overall plume structures remain largely unaffected. Over  
458 Beijing, the simulations using the ODIAC inventory (Figs. 7e, f) display an almost identical fXCO<sub>2</sub> enhancement distribution across  
459 different wind conditions, showing pronounced anomalies in the urban area. Such similarity is unrealistic.

460 We attribute this behavior to the ODIAC inventory allocating disproportionately high fossil fuel emissions to central Beijing.  
461 When STILT footprints intersect the urban area, the high emission gradients in ODIAC (central urban emissions far exceeding  
462 suburban values) amplify fXCO<sub>2</sub> enhancements in the inner city. ODIAC's low-emission thresholds are influenced by nighttime  
463 light saturation, with median differences ranging from 47% to 84%. Consequently, ODIAC artificially concentrates emissions in the  
464 city center while underrepresenting surrounding suburban areas. This makes it challenging to accurately constrain CO<sub>2</sub> fluxes in the  
465 peripheral regions using ODIAC. Observations from the TCCON Xianghe site further highlight the limitations of ODIAC's emission  
466 allocation in the Beijing area.



467  
 468 **Figure 8 Comparison of fXCO<sub>2</sub> observed at the TCCON Xianghe site in Beijing during August with fXCO<sub>2</sub> simulated using the NO<sub>x</sub>**  
 469 **inventory and the ODIAC inventory. Panel (a) shows the fXCO<sub>2</sub> observed by TCCON (red line), simulated fXCO<sub>2</sub> using the NO<sub>x</sub>**  
 470 **emissions (dark blue line), simulated fXCO<sub>2</sub> using the ODIAC inventory (light blue line), and simulated fXCO<sub>2</sub> using the posterior NO<sub>x</sub>**  
 471 **emissions (green line). Panel (b) presents the distribution of differences between simulated fXCO<sub>2</sub> (from the NO<sub>x</sub> and ODIAC inventories)**  
 472 **and TCCON observations throughout August, with bold numbers indicating the mean and standard deviation. Panel (c) shows the**  
 473 **cumulative probability distributions of the differences between simulated fXCO<sub>2</sub> (NO<sub>x</sub> emissions and ODIAC inventory) and TCCON**  
 474 **observations.**

475  
 476 Figure 8 presents the comparison of August fXCO<sub>2</sub> at the TCCON site with simulations using the ODIAC and NO<sub>x</sub> inventories.  
 477 Unlike the fXCO<sub>2</sub> calculation described in Section 2.2.2, the TCCON observations provide daily-averaged fossil fuel CO<sub>2</sub>  
 478 enhancements, where TCCON fXCO<sub>2</sub> is calculated as TCCON XCO<sub>2</sub> minus background XCO<sub>2</sub> and NEE contributions (details in  
 479 the Appendix A3). In Figure 8a, the dark blue line represents fXCO<sub>2</sub> simulated at the TCCON site using the NO<sub>x</sub> inventory, the  
 480 green line shows the fXCO<sub>2</sub> simulated after optimization with the inversion using DQ-1 observations, the light blue line corresponds  
 481 to ODIAC-based simulations, and the red line depicts TCCON-observed fXCO<sub>2</sub>.

482 Figure 8b quantifies the accuracy of the simulations by plotting the difference between the simulated ffXCO<sub>2</sub> and TCCON  
 483 observations on the same day and summarizing the monthly mean and standard deviation. The monthly mean absolute difference  
 484 for the NO<sub>x</sub> inventory is 0.82 ppm, while ODIAC exhibits a much larger discrepancy of 5.19 ppm. The inversion-constrained NO<sub>x</sub>  
 485 inventory reduces the mean absolute difference to 0.52 ppm, closely matching TCCON observations. Figure 8c shows the  
 486 cumulative probability distribution of the differences between simulated and observed ffXCO<sub>2</sub>. The differences for the NO<sub>x</sub> and  
 487 inversion-constrained NO<sub>x</sub> simulations are largely centered around zero (blue and red lines), whereas for ODIAC, approximately  
 488 30% of differences exceed 5 ppm.

489 These results indicate that for Beijing in August, simulations based on the NO<sub>x</sub> inventory outperform those using ODIAC.  
 490 Given that the prior ffCO<sub>2</sub> emissions in both inventories are of similar magnitude, the observed discrepancies are primarily  
 491 attributable to the spatial allocation of emissions in ODIAC. The combined inversion using TROPOMI and ACDL data provides a  
 492 more accurate reconstruction of urban ffXCO<sub>2</sub> plume structures.

### 493 3.2.3. ffCO<sub>2</sub> Inversion Results

494 Table 2 Results of inversion of for CO<sub>2</sub>-to-NO<sub>x</sub> ratio selected cities using DQ-1 XCO<sub>2</sub> data

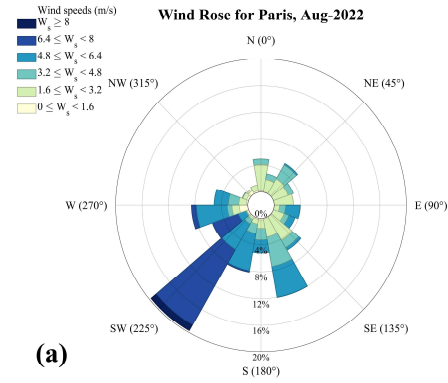
City	Overpass	Prior CO <sub>2</sub> -to- NO <sub>x</sub> ratio ( $\lambda$ )	Prior uncertainty (%)	Observation uncertainty (ppm)	Model transport uncertainty (ppm)	Posterior CO <sub>2</sub> -to-NO <sub>x</sub> ratio ( $\lambda$ ) and uncertainty
Cairo	2022/08/02	470	40.59%	1.23	1.75	428±64.58
	2022/08/19			1.06	2.10	512±96.56
Paris	2022/08/07	601	30.12%	2.45	0.36	731±107.60
	2022/08/21			1.68	0.76	742±138.53
Beijing	2022/08/09	694	28.12%	2.31	1.28	640±90.11
	2022/08/16			1.79	3.25	553±89.80

495 This section presents the inversion results of urban carbon emissions for Cairo, Paris, and Beijing, based on TROPOMI and  
 496 DQ-1 satellite overpass observations (see Table 2). In the inversion, we systematically accounted for observational errors and  
 497 uncertainties in atmospheric transport to improve the reliability of the emission estimates. From the posterior results, we derived  
 498 city-specific CO<sub>2</sub>-to-NO<sub>x</sub> ratios and, by combining them with TROPOMI-derived NO<sub>x</sub> emissions, further quantified fossil fuel CO<sub>2</sub>  
 499 (ffCO<sub>2</sub>) emissions. This approach not only enables quantitative assessment of emissions but also provides a scientific basis for cross-  
 500 city comparisons of emission characteristics, while demonstrating the potential of multi-satellite data for urban emission monitoring.

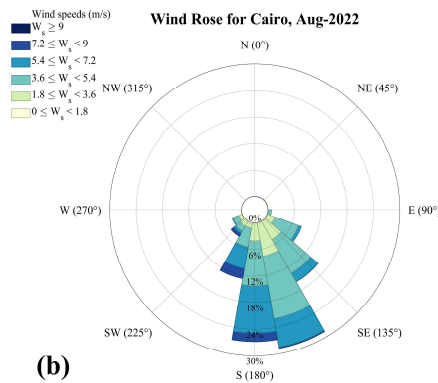
501 For the selected orbits, the posterior CO<sub>2</sub>-to-NO<sub>x</sub> ratios were 428–512 for Cairo, 731–742 for Paris, and 553–640 for Beijing

502 (Table 2). These ratios exhibited clear temporal variability under different background conditions. The magnitude of emissions  
503 captured by each orbit depended strongly on its distance from major emission regions and the contemporaneous domain-averaged  
504 wind conditions(Che et al., 2022). The domain-averaged wind speeds for the study month (Fig. 9), as well as the high-resolution  
505 wind fields at overpass time (black arrows in Figs. 5–7), were consistently greater than  $3 \text{ m s}^{-1}$ . Under such meteorological conditions,  
506 the posterior estimates represent emissions from several hours prior to satellite overpass. The posterior uncertainties of the  $\text{CO}_2$ -to-  
507  $\text{NO}_x$  ratio were 15.09%–18.86% for Cairo, 14.72%–18.67% for Paris, and 14.08%–16.24% for Beijing. Overall, uncertainties were  
508 larger for Cairo and Paris compared with Beijing.

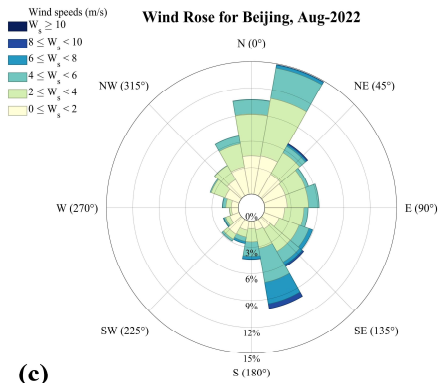
509 As described in section 4.1, the prior uncertainty of the  $\text{CO}_2$ -to- $\text{NO}_x$  ratio was prescribed based on available statistics and  
510 emission characteristics. Owing to more comprehensive statistics and advanced manufacturing processes, large metropolitan areas  
511 typically exhibit better-characterized emission features. Accordingly, the prior uncertainties for Beijing and Paris were smaller than  
512 those for Cairo. Table 2 further shows that the relative contributions of observational and transport errors differed across cities. In  
513 Cairo, transport errors dominated over observational errors, whereas in Paris the opposite held true. For Beijing, the relative  
514 magnitudes of transport and observational errors varied across orbits. The overall smaller posterior uncertainty for Beijing compared  
515 to Cairo and Paris reflects its more stable prior emission characteristics.



(a)



(b)



(c)

Figure 9 Monthly mean wind rose plots for Cairo, Paris, and Beijing in August.

### 3.3. The Uncertainty of Transport Model

Atmospheric transport modeling uncertainty has been recognized as a major factor affecting emission constraints (Wu et al., 2018). Systematic errors arising from a combination of transport model biases and misrepresented statistical inputs can reduce the magnitude and spatial coverage of terrestrial uncertainty reductions by roughly a factor of two. Notably, transport-related uncertainties in fXCO<sub>2</sub> represent a key source of error in inverse emission estimates (Ye et al., 2020). In this section, we quantify the impact of transport errors on simulated XCO<sub>2</sub> arising from uncertainties in horizontal wind fields and vertical mixing, with a focus on their influence on the inversion of fXCO<sub>2</sub> fluxes.

Errors induced by wind field uncertainties propagate through the model and affect the accuracy of CO<sub>2</sub> emission estimates (Sheng et al., 2025). Previous studies have accounted for column transport errors by weighting variance relative to pressure and treating each model level independently (Lin and Gerbig, 2005; Wu et al., 2018). Ye et al. 2020 further quantified fXCO<sub>2</sub>

simulation uncertainty by introducing random perturbations in wind speed and direction (Ye et al., 2020). Building on these approaches, we investigate how horizontal wind speed and wind direction errors influence inversion performance.

Here, horizontal transport error is propagated through the model via its effect on fXCO<sub>2</sub> plume dispersion (Luo et al., 2026; Qu et al., 2026). For the selected cities, errors are assumed to be unbiased. Wind direction uncertainty is represented by rotating the plume around the emission center, followed by the addition of random wind speed perturbations to the rotated plume. Using DQ-1 wind field data, random errors were added at each model level (wind direction perturbation between -10° and 10°, wind speed perturbation between -1 m/s and 1 m/s), and the STILT footprints were recomputed to obtain plume-averaged footprints with random errors included (Yi et al., 2024).

In total, 10<sup>4</sup> simulations were conducted, with the fXCO<sub>2</sub> integrated along each satellite track. The standard deviation (1σ) of these simulations is used to represent the uncertainty in simulated fXCO<sub>2</sub> resulting from horizontal transport errors (Figure 10).

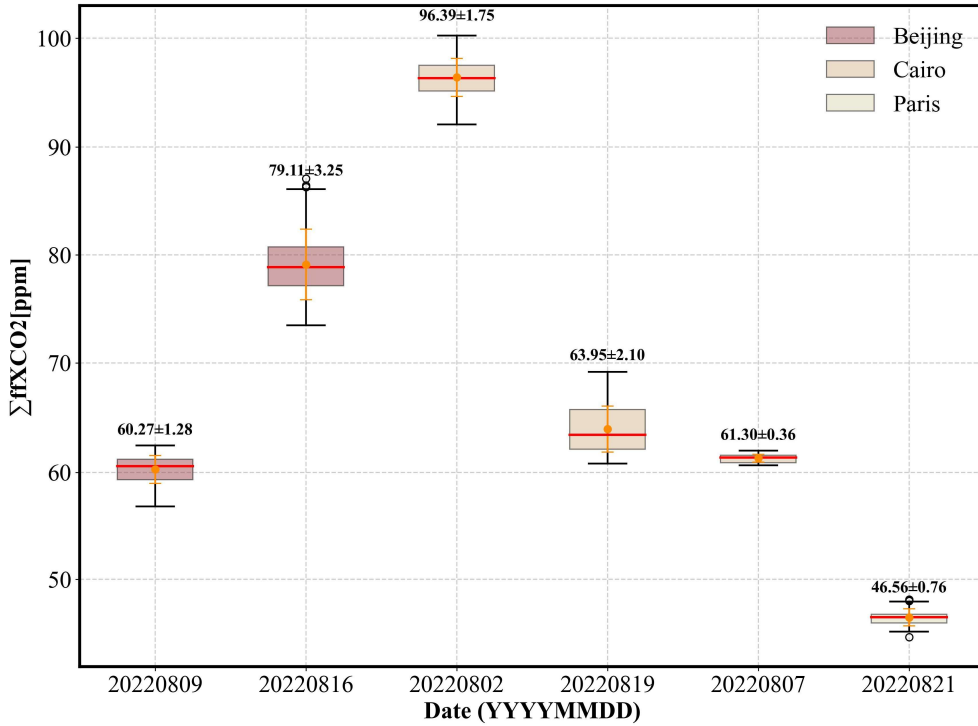


Figure 10 Boxplots of modeled integrated fXCO<sub>2</sub> enhancements fXCO<sub>2</sub> along selected DQ-1 overpasses for the three cities (distinguished by box color) with dates labeled on the x-axis. For each box, the central line represents the median (q<sub>2</sub>), and the bottom and top edges represent the 25th and 75th percentiles (q<sub>1</sub> and q<sub>3</sub>), respectively. Whiskers extend to the minimum and maximum values. Numbers indicate the mean ± standard deviation.

544 Figure 10 presents the total simulated fXCO<sub>2</sub> along DQ-1 overpasses for the different study regions. Overall, the simulated  
545 fXCO<sub>2</sub> totals for the three cities are of comparable magnitude. Notably, compared with Beijing and Cairo, the horizontal transport  
546 uncertainty along the two Parisian tracks is the lowest, at 0.36 ppm and 0.76 ppm, respectively. In Cairo, the satellite tracks traverse  
547 the edges of emission plumes, making the simulations highly sensitive to wind speed and direction, which results in larger transport  
548 model errors. Beijing, with its complex terrain and variable wind fields, exhibits more intricate transport uncertainties relative to  
549 the other two cities. These observations indicate that transport model uncertainty is closely related to city-scale emissions, the  
550 relative alignment of plumes and satellite tracks, model performance, and local topography. Variations in these factors contribute to  
551 temporal changes in posterior emission uncertainties along different tracks.

552 Vertical turbulent mixing governs the vertical transport of air parcels and controls the dilution of surface emissions within the  
553 boundary layer (Vertical mixing in atmospheric tracer transport models: error characterization and propagation). Although column-  
554 integrated measurements may be less sensitive to the vertical distribution of tracers than in situ observations, errors in planetary  
555 boundary layer (PBL) height can still affect column simulations due to wind shear and its interaction with vertical redistribution of  
556 tracers (Planetary boundary layer errors in mesoscale inversions of column-integrated CO<sub>2</sub> measurements). It is worth noting that  
557 the ACDL instrument includes an aerosol channel capable of providing extinction coefficient profiles and planetary boundary layer  
558 height (PBLH) products (Dai et al., 2024). In this study, PBLH data derived from ACDL retrievals are used in the simulations,  
559 helping to mitigate errors arising from inaccurate boundary layer height assumptions. Therefore, boundary layer height errors are  
560 not considered in the estimation of fXCO<sub>2</sub>.

#### 561 4. Importance of Satellite Observations for Optimizing the CO<sub>2</sub>-to-NO<sub>x</sub> Ratio

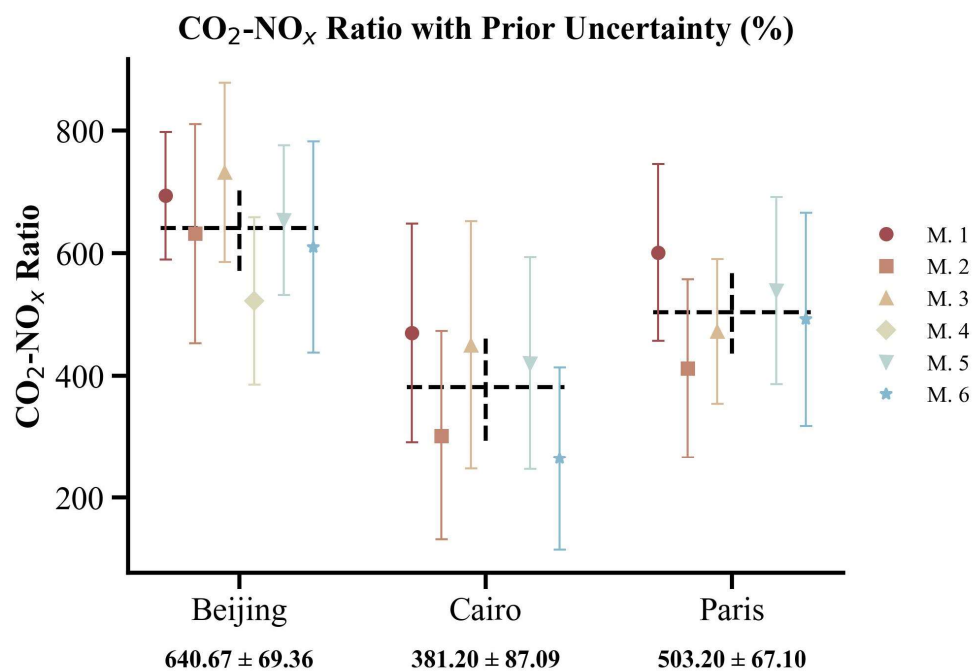
##### 562 4.1. Variations in CO<sub>2</sub>-to-NO<sub>x</sub> ratio calculation methods

563 We systematically accounted for the uncertainties associated with the prior CO<sub>2</sub>-to-NO<sub>x</sub> ratios for each method (see Section  
564 2.2.1 (4) M1-M6). The uncertainty of the CO<sub>2</sub>-to-NO<sub>x</sub> ratio arises from the uncertainties of the underlying emissions. For Method  
565 1, a Monte Carlo simulation was performed: CO<sub>2</sub> and NO<sub>x</sub> inventory uncertainties (Wang et al., 2013) were used to generate random  
566 perturbations at each grid, and the CO<sub>2</sub>-to-NO<sub>x</sub> ratio was recalculated 10,000 times to obtain the distribution characteristics. The  
567 prior CO<sub>2</sub>-to-NO<sub>x</sub> ratio uncertainty was expressed as R90/M, where R90 is the range between the 95th and 5th percentiles and M is  
568 the median value from 10,000 Monte Carlo simulations. For Method 2, the uncertainty was represented as:

$$569 \sigma_{C/N} = \sqrt{\sigma_{NO_x}^2 + \sigma_{FFCO_2}^2} \quad (14)$$

570 where  $\sigma_{NO_x}$  and  $\sigma_{FFCO_2}$  denote the uncertainties of the NO<sub>x</sub> and fXCO<sub>2</sub> emission factors, respectively. Notably, for each  
571 method, the use of different inventories requires adjustment of the assigned uncertainties (see Appendix A6). In Method 3, the prior

572 CO<sub>2</sub>-to-NO<sub>x</sub> ratio uncertainty was derived from the quadratic sum of observational uncertainties in NO<sub>2</sub> and CO<sub>2</sub> concentrations and  
 573 the Gaussian fitting uncertainty.



574  
 575 **Figure 11 Results of CO<sub>2</sub>-to-NO<sub>x</sub> ratios obtained using different calculation methods for Beijing, Cairo, and Paris. Different CO<sub>2</sub>-to-NO<sub>x</sub>**  
 576 **ratios within the same city are distinguished by color. Additionally, the mean and standard deviation of the different ratios for each city**  
 577 **are also shown.**

578  
 579 In this section, we used six different CO<sub>2</sub>-to-NO<sub>x</sub> ratio calculation methods to estimate the city-scale ratios for Beijing, Cairo,  
 580 and Paris in August. Since the MEIC inventory is only available for Beijing, six prior CO<sub>2</sub>-to-NO<sub>x</sub> ratios were obtained for Beijing,  
 581 while five ratios were derived for Paris and Cairo. Figure 11 presents the CO<sub>2</sub>-to-NO<sub>x</sub> ratios and their associated uncertainties for  
 582 each city using the different methods. We also calculated the mean and standard deviation of the ratios across methods for each city,  
 583 reflecting both the overall understanding of the city-scale prior CO<sub>2</sub>-to-NO<sub>x</sub> ratio and the variability arising from methodological  
 584 differences.

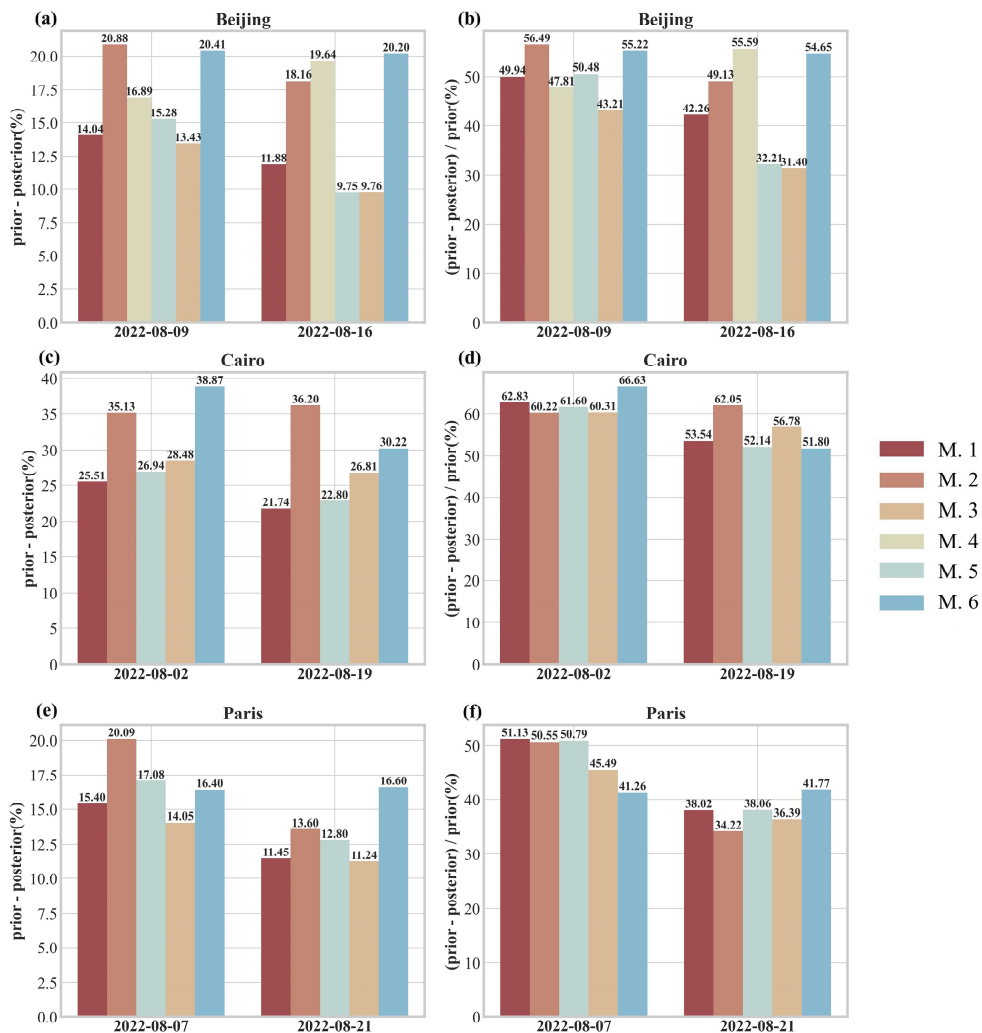
585 The results consistently show the ordering Beijing > Paris > Cairo. Moreover, more developed cities typically have better  
 586 production technologies and more detailed emission statistics(Oda et al., 2019; Ye et al., 2020). Consequently, the prior uncertainties  
 587 for Beijing and Paris are notably smaller than those for Cairo, and the variability of CO<sub>2</sub>-to-NO<sub>x</sub> ratios across methods is also reduced

588 for these cities.

#### 589 **4.2. Bayesian Inversion for Reducing CO<sub>2</sub>-to-NO<sub>x</sub> Ratio Uncertainty**

590 Using different prior CO<sub>2</sub>-to-NO<sub>x</sub> ratios, we conducted the Bayesian inversion described in Section 2.2.2 to optimize the August  
591 CO<sub>2</sub>-to-NO<sub>x</sub> ratios for Beijing, Cairo, and Paris along the respective DQ-1 satellite overpasses. Figure 12 shows the absolute  
592 reduction in posterior uncertainty (posterior minus prior) and the relative reduction (prior minus posterior, divided by prior) for each  
593 city across different orbits. For Beijing, the posterior uncertainty decreased by 9.75%–20.88%, corresponding to a 31.4%–56.49%  
594 reduction relative to the prior. In Cairo, the posterior uncertainty decreased by 21.74%–38.87%, equivalent to a 51.8%–66.63%  
595 reduction, while in Paris the reduction ranged from 11.24% to 20.09%, corresponding to a 34.22%–51.13% decrease relative to the  
596 prior.

597 These results indicate that, for all cities, the posterior uncertainties were significantly reduced regardless of the method used to  
598 calculate the prior ratio. This demonstrates that constraining the inversion with DQ-1 ACDL observations substantially improves  
599 the accuracy of ffCO<sub>2</sub> estimates derived from NO<sub>x</sub> emissions. Notably, in Cairo—the city with the largest prior uncertainty—the  
600 reduction in uncertainty after constraining with both active and passive satellite observations was the greatest, highlighting the  
601 effectiveness of satellite data in mitigating emission uncertainties in cities with incomplete statistical information. These findings  
602 underscore the potential of satellite remote sensing to supplement emission inventories and enhance the reliability of urban emission  
603 estimates.

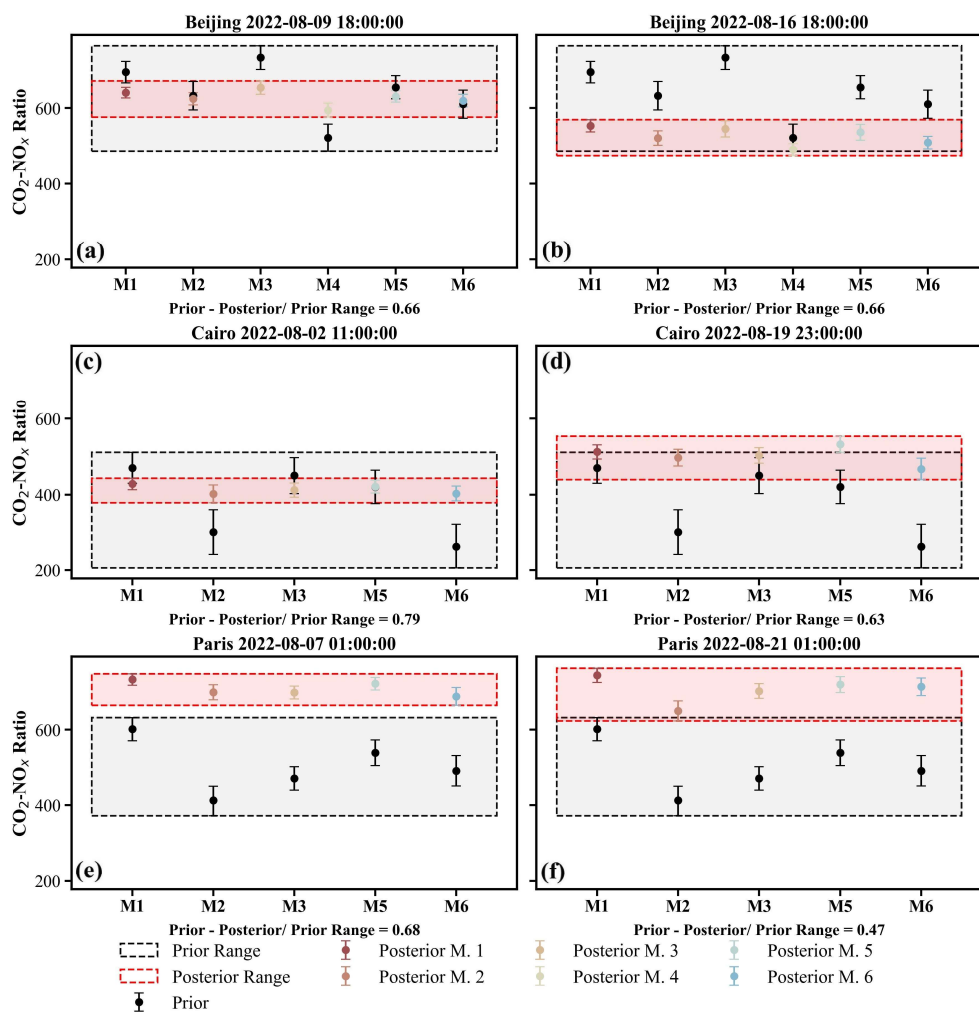


604  
 605 **Figure 12 Comparison of Bayesian inversion prior and posterior uncertainties for each orbit over different cities. Panels (a), (c), and (e)**  
 606 **show the absolute reduction in uncertainty (prior uncertainty minus posterior uncertainty), while panels (b), (d), and (f) show the relative**  
 607 **reduction in uncertainty (prior minus posterior uncertainty divided by prior uncertainty). Results from different prior CO<sub>2</sub>-to-NO<sub>x</sub> ratios**  
 608 **are represented by bars in different colors, with the values displayed at the top of each bar.**

609  
 610 Furthermore, we examined the range of CO<sub>2</sub>-to-NO<sub>x</sub> ratios calculated for each city using different methods (Fig. 13). In the  
 611 figure, the black boxes represent the prior distribution ranges, while the red boxes indicate the posterior distribution ranges. The  
 612 distribution ranges illustrate the variability among CO<sub>2</sub>-to-NO<sub>x</sub> ratios obtained from different methods, and we also quantified the

613 reduction of the posterior range relative to the prior. Except for the orbit over Paris on 21 August, all other results show that the  
 614 posterior ranges were reduced by more than 60% compared to the priors.

615 These results demonstrate that our approach effectively reduces the discrepancies arising from different CO<sub>2</sub>-to-NO<sub>x</sub> ratio  
 616 calculation methods. That is, prior ratios derived from various methods are constrained to approximately the same range after  
 617 inversion. This finding underscores the importance of using observational constraints to obtain more accurate CO<sub>2</sub>-to-NO<sub>x</sub> ratios in  
 618 future ffCO<sub>2</sub> emission estimations.



619  
 620 **Figure 13** Distribution ranges of prior and posterior CO<sub>2</sub>-to-NO<sub>x</sub> ratios calculated using different methods. Black boxes represent the  
 621 range of prior CO<sub>2</sub>-to-NO<sub>x</sub> ratios, with posterior ratios indicated by black circles. Red boxes represent the range of posterior CO<sub>2</sub>-to-NO<sub>x</sub>

ratios, with posterior uncertainties from different methods shown using different colors and symbols.

## 5. Summary

Accurate identification and quantification of anthropogenic CO<sub>2</sub> emissions form a critical scientific basis for national emission reduction policies and carbon sink strategies. However, bottom-up inventory approaches typically operate on long compilation cycles (e.g., annual), making it difficult to capture short-term or near-real-time emission dynamics. Most inventories provide only annual totals and lack the temporal resolution needed to characterize daily, hourly, or event-driven emissions.

In this study, we developed a city-scale ffCO<sub>2</sub> inversion framework that integrates both active and passive satellite observations of greenhouse gases. This framework enables high-resolution estimation of fossil fuel emissions at satellite overpass times and over preceding hours, while simultaneously constraining the city-scale CO<sub>2</sub>-to-NO<sub>x</sub> ratio. A key feature of the approach is its reduced reliance on prior emission inventories, allowing rapid and objective identification and quantification of anthropogenic emission signals at regional scales, thereby enhancing the monitoring and verification of urban emission dynamics. In this framework, satellite-observed XCO<sub>2</sub> enhancements attributed to urban emissions are used to constrain WRF-STILT atmospheric transport simulations of anthropogenic CO<sub>2</sub>. This process not only enables quantitative assessment of urban fossil fuel emissions but also provides independent evidence for improving emission inventories and refining urban carbon accounting systems. The study highlights the potential of combining multi-source satellite observations with transport models and lays a foundation for future city-scale ffCO<sub>2</sub> inversions based on the CO<sub>2</sub>-to-NO<sub>x</sub> ratio. Furthermore, we discuss the impact of the lack of standardized CO<sub>2</sub>-to-NO<sub>x</sub> ratio calculation methods on urban emission estimates and demonstrate that observational constraints on city-scale ratios can substantially improve ffCO<sub>2</sub> estimation from a carbon-nitrogen co-optimization perspective. Using a Bayesian inversion approach, we optimized the CO<sub>2</sub>-to-NO<sub>x</sub> ratios for Cairo, Paris, and Beijing in August 2022 based on DQ-1 satellite overpasses and estimated the cities' fossil fuel CO<sub>2</sub> emissions using TROPOMI NO<sub>2</sub> data. The resulting CO<sub>2</sub>-to-NO<sub>x</sub> ratios ranged from 428–512, 731–742, and 553–640 for Cairo, Paris, and Beijing, respectively, indicating significant day-to-day variability in emission estimates. Cairo exhibited the largest posterior uncertainty, primarily due to high prior uncertainty and transport model errors. Differences in posterior uncertainties across orbits were also closely related to meteorological conditions and the relative position of the satellite tracks to urban plumes. We further compared ffXCO<sub>2</sub> enhancement distributions simulated using the ODIAC inventory. Results for Cairo and Paris were broadly consistent with TROPOMI-based simulations, while notable differences emerged for Beijing. TCCON XCO<sub>2</sub> observations were used to interpret these discrepancies. The monthly mean ffXCO<sub>2</sub> enhancement derived from TROPOMI NO<sub>2</sub> data differed from TCCON measurements by less than 1 ppm, whereas the ODIAC-based results deviated by 5.16 ppm. This highlights the need to account for uncertainties arising from inventory allocation and outdated updates when interpreting XCO<sub>2</sub> inversion results. We systematically examined the impact of different prior CO<sub>2</sub>-to-NO<sub>x</sub> ratio calculation methods on urban ffCO<sub>2</sub> inversions. In our study, methodological differences led to variations of 10.8%–22.8% in prior ratios. Importantly, regardless of the prior ratio

652 or its uncertainty, DQ-1 observations constrained the posterior values to a similar range, substantially reducing discrepancies among  
653 different calculation methods. Another limitation concerns the uncertainty of the divergence-derived NO<sub>x</sub> emissions. Although  
654 monthly averaging reduces random noise, it does not guarantee that daily divergence errors average to zero. Sampling biases related  
655 to clouds, aerosols, surface reflectance, and photochemical variability may persist in the monthly mean. Moreover, gradient  
656 operations can amplify white noise in the NO<sub>2</sub> column field and generate structured artifacts in the derived fluxes. Therefore, the  
657 current uncertainty estimates should be interpreted as lower-bound, first-order uncertainty estimates. Future work should include  
658 more explicit noise-filtering and detection-limit analyses, ideally using ensemble perturbations of the original Level-2 NO<sub>2</sub>  
659 observations and high-resolution chemical transport simulations to better represent NO<sub>2</sub> profile shapes, lifetimes, and NO<sub>x</sub>:NO<sub>2</sub>  
660 conversion factors. {Cifuentes, 2025 #92; Guan, 2026 #95; Wang, 2025 #91; Zhang, 2026 #96}

661 Looking ahead, improving satellite-based city-scale ffCO<sub>2</sub> inversions will require accounting for the spatiotemporal  
662 correlations of prior emission errors. Our current framework does not yet incorporate this aspect, which imposes certain limitations  
663 on the interpretation and application of the results. Satellite observations are inherently constrained by inversion errors, sampling  
664 geometry, and revisit frequency, limiting overpass opportunities. A single prior factor, such as a uniform CO<sub>2</sub>-to-NO<sub>x</sub> ratio, cannot  
665 fully capture the complex spatiotemporal features of emissions. Incorporating prior error correlations can mitigate uncertainties  
666 arising from sparse observations and better resolve temporal and spatial variability in urban emissions. Moreover, the number of  
667 satellite tracks required to constrain city emissions depends on the desired emission resolution and uncertainty thresholds relevant  
668 for policy applications. Lower temporal resolution may suffice for long-term trend analysis, whereas capturing short-term peaks or  
669 episodic emissions necessitates higher observation frequency and precision. This consideration aligns with emerging international  
670 approaches emphasizing multi-platform, multi-temporal observations, combining polar-orbiting, geostationary satellites, and  
671 ground-based monitoring to achieve multidimensional constraints on urban emissions.

672 Overall, our results demonstrate that coupling high-resolution atmospheric transport simulations with a Bayesian inversion  
673 framework allows TROPOMI and DQ-1 multi-source observations to effectively constrain urban ffXCO<sub>2</sub> enhancement signals. The  
674 approach captures spatial heterogeneity of emissions, particularly in cities with strong emission intensities and well-defined plume  
675 structures, providing a robust basis for quantitative analysis. Furthermore, current methods estimating ffCO<sub>2</sub> from NO<sub>x</sub> emissions  
676 often lack explicit treatment of CO<sub>2</sub>-to-NO<sub>x</sub> ratio uncertainty, which can significantly influence inversion outcomes. Differences  
677 among calculation methods for the same region can be as large as 258–304. Notably, our inversion framework substantially reduces  
678 CO<sub>2</sub>-to-NO<sub>x</sub> ratio uncertainty, providing more stable priors for urban ffCO<sub>2</sub> estimation. Recent studies suggest the need to further  
679 optimize CO<sub>2</sub>-to-NO<sub>x</sub> emission ratios at regional scales to improve ffCO<sub>2</sub> estimates (Feng et al., 2024). Therefore, we recommend  
680 that future NO<sub>x</sub>-based ffCO<sub>2</sub> inversion studies adopt observational constraints to refine CO<sub>2</sub>-to-NO<sub>x</sub> ratios, minimizing errors arising  
681 from prior ratio uncertainties.

682 **Appendix**

683 **A1: ACDL XCO<sub>2</sub> Data Inversion**

684 Unlike passive satellite XCO<sub>2</sub> products (e.g., OCO-2/3), the DQ-1 XCO<sub>2</sub> product—hereafter referred to as  $XCO_2^{Lidar}$  to  
 685 distinguish it from passive measurements—is derived from the differential absorption between ACDL’s on-band wavelength (strong  
 686 CO<sub>2</sub> absorption) and off-band wavelength (weak CO<sub>2</sub> absorption). Here, “WF(p)” refers to the lidar signal and integrated weighting  
 687 function introduced in Section 2.1.1.1, with “p” representing atmospheric pressure:

$$688 \quad XCO_2^{Lidar} = \frac{2 \cdot \ln \left( \frac{V_{off} V_{on-0}}{V_{on} V_{off-0}} \right)}{\int_{p_{surface}}^{p_{toa}} WF(p) dp} \quad (A1)$$

689 Here,  $V_{on}$  and  $V_{off}$  denote the reflected signal energies at the on-band and off-band wavelengths, respectively, while  $V_{on-0}$   
 690 and  $V_{off-0}$  correspond to the transmitted signal energies.  $p_{surface}$  represents the atmospheric pressure at the sub-satellite point  
 691 of the laser, and  $p_{toa}$  denotes the pressure at the top of the atmosphere. The denominator in Equation A1 represents the integrated  
 692 weighting function (WF(p)), which can be expressed according to (Refaat et al., 2016) as:

$$693 \quad WF(p) = \Delta\sigma_{wf}(\lambda_{on}, \lambda_{off}, p) \cdot N_{dry}(p) \quad (A2)$$

694 Here,  $\Delta\sigma_{wf}(\lambda_{on}, \lambda_{off}, p)$  represents the differential absorption cross-section of CO<sub>2</sub> between the on-band  $\lambda_{on}$  and off-band  $\lambda_{off}$   
 695 wavelengths at pressure p.  $N_{dry}$  denotes the number of dry air molecules per unit area within the corresponding pressure layer.

696  
 697 **Table A1 DQ-1 ACDL operating parameters**

Parameters	Values
Orbit altitude	705km
Lidar footprint diameter	~70m
Horizontal spacing of lidar footprints	~350m
Field of view	<0.2mrad
Telescope diameter	1000nm
Divergence angle after laser beam expansion	<0.1mrad
Repetition frequency	20Hz
Laser pulse width	<50ns
Laser energy	75mJ
Off-line wavelength	1572.085nm

## A2: Derivation of the Principle of Mass Balance

For satellite column observations of specific species such as NO<sub>2</sub>, the mass balance equation can be expressed as follows:

$$\begin{cases} \frac{\partial V_{NO_2}}{\partial t} + \nabla \cdot \vec{F}_{NO_2} = E_{NO_2} - S \\ \vec{F}_{NO_2} = V_{NO_2} \vec{u}_{100} \\ S \approx \frac{V_{NO_2}}{\tau} \end{cases} \quad (A3)$$

Here,  $V_{NO_2}$  represents the columnar NO<sub>2</sub> concentration observed by TROPOMI, defined as a scalar function of  $x$  and  $\nabla = (\frac{\partial}{\partial x}, \frac{\partial}{\partial y})$  denotes the gradient operator;  $\vec{F}_{NO_2} = (F_x, F_y)^T$  is the horizontal flux, with units of mol·m<sup>-2</sup>·s<sup>-1</sup>, expressed as a vector function of  $x$  and  $y$  and weighted by the wind vector. The 100 m wind field is commonly used to characterize horizontal transport within the planetary boundary layer (PBL)(Sun, 2022).  $\tau$  represents the first-order chemical lifetime of NO<sub>2</sub> in seconds.

By solving the system of equations in Equation A3 and expanding the horizontal flux divergence using vector calculus, we obtain the derivation of Equation A4 from Equation A3:

$$\begin{cases} \vec{u}_{100} \cdot (\nabla V_{NO_2}) + V_{NO_2} (\nabla \cdot \vec{u}_{100}) = \nabla \cdot \vec{F}_{NO_2} \\ E_{NO_2} = \frac{\partial V_{NO_2}}{\partial t} + \nabla \cdot \vec{F}_{NO_2} + \frac{V_{NO_2}}{\tau} \end{cases} \quad (A4)$$

Sun et al. 2022, in their first-principles derivation, introduced a "topographic correction term" to replace the wind divergence term  $V_{NO_2}(\nabla \cdot \vec{u}_{100})$ . Beirle et al. 2023 demonstrated that incorporating a topographic correction significantly improves the inversion of power-plant NO<sub>x</sub> emissions based on the divergence method. Koene et al. 2024 carefully compared these two terms in the derivation of the divergence method, showing that they originate from the continuity equations of the source and non-source terms, and that numerically, the wind divergence and wind-topography terms are approximately equal in the absence of observational errors.

Despite their numerical equivalence in derivation, the accuracy of reanalyzed wind fields is generally lower than that of surface elevation data. Therefore, in practical measurements—particularly in complex, fine-scale settings—the wind divergence term alone may not provide sufficient constraint. Correcting wind divergence artifacts using topographic gradients is more feasible, especially in regions with rugged terrain. Accordingly, we revise Equation A5 using Equation A4 as follows:

$$\frac{V_{NO_2} \vec{u}_{10} \cdot (\nabla z_0)}{H} \approx V_{NO_2} (\nabla \cdot \vec{u}_{100}) \quad (A5)$$

Here,  $\frac{V_{NO_2} \vec{u}_{10} \cdot (\nabla z_0)}{H}$  represents the topographic correction term, where the 10 m wind is approximated as the near-surface wind,

721 and  $H$  denotes the gas scale height in meters. Following previous studies (Beirle et al., 2023; Sun, 2022; Liu et al., 2021), Equation  
722  $A_5$  is assimilated over both temporal and spatial dimensions. This procedure is concisely represented using the operator  $(f)$ , as  
723 introduced in the derivations by Liu et al. and Sun et al. Ultimately, this approach allows the derivation of the vertical  $\text{NO}_2$  flux on  
724 a grid-resolved basis.

### 725 **A3: Atmospheric Model Setting**

726 In this study's application of STILT, hourly outputs from version 4.0 of WRF are used to provide high resolution meteorological  
727 fields, with the model grid configured to 32 vertical (eta) layers. The 6-hourly NCEP FNL (Final) global operational analysis data  
728 ( $\text{ds083.3}$ ,  $0.25^\circ \times 0.25^\circ$ ) are used as initial and boundary conditions for meteorological and land surface fields to provide the  
729 initial and boundary conditions for WRF runs. The simulations run for 30 hours, but only the 7th to 30th hours of each simulation  
730 are used to avoid spin-up effects in the first 6 hours.

731 In this study, we used the STILT model, version 2, to simulate atmospheric transport processes. STILT is configured to release  
732 500 particles per receptor each time, with forward dispersion over 24 hours. The particle release heights for STILT are set within  
733 the range of 50-1000 m, with releases every 50 m, and 1000-2000 m, with releases every 100 m, the spatial resolution of the STILT  
734 simulations is  $1 \text{ km} \times 1 \text{ km}$ . Generally, as MAXAGL increases from 1 km to 2 km, the urban enhancement increases and then  
735 stabilizes.

736 **Table A2 Model version information used in this study**

Model	Version
STILT(Stochastic Time-Inverted Lagrangian Transport)	V2
WRF(Weather Research and Forecasting)	V4.0
X-STILT(X-Stochastic Time-Inverted Lagrangian Transport model)	V1

737

### 738 **A4: Calculation of NEE $\text{XCO}_2$ enhancement**

739 We performed vertical integration following the method provided by the TCCON team, using the 51 altitude levels listed in  
740 the publicly available `ak_altitude` dataset, which also serve as input heights for the STILT model. In contrast to the XSTILT  
741 calculation method used for DQ-1, we applied the integration operator `integration_operator_x2019` together with the mean averaging  
742 kernel `ak_xco2` to the STILT footprints across the 51 levels in order to generate the simulated XSTILT values required for this study.  
743 We selected the National Institute for Environmental Studies (Japan) data-driven Upscale Product of Global Gross Primary  
744 Production (NEE) as the reference for the overall local NEE during the DQ-1 overpasses. By convolving the NEE inventory with

745 XSTILT, we simulated the XCO<sub>2</sub> enhancement at TCCON sites attributable to NEE.

#### 746 **A5: Calculation of Prior NO<sub>x</sub> Emission Uncertainty**

747 The uncertainty estimated here should be regarded as a first-order propagated uncertainty rather than the full uncertainty of the  
748 divergence-derived NO<sub>x</sub> emissions. In particular, this formulation does not fully capture structured errors arising from finite-  
749 difference gradient operators, oversampling from Level-2 observations to Level-3 grids, non-Gaussian retrieval noise, or sampling  
750 biases caused by clouds, aerosols, surface reflectance, and photochemical variability. The uncertainty of the NO<sub>x</sub> inventory derived  
751 from the mass balance approach can be estimated using the error propagation law as follows:

$$752 \quad \varepsilon_{NO_x} = \sqrt{\varepsilon_\alpha^2 + \varepsilon_{NO}^2} \quad (A6)$$

753 where  $\varepsilon_\alpha$  represents the uncertainty in the NO<sub>x</sub>/NO<sub>2</sub> ratio, its uncertainty arises from the uncertainties in the input parameters  
754 of the chemical model(Liu et al., 2022). And  $\varepsilon_{NO_2}$  denotes the uncertainty in the NO<sub>2</sub> flux field. The latter can be further  
755 decomposed as:

$$756 \quad \varepsilon_{NO_2} = \sqrt{\varepsilon_{TROPOMI}^2 + \varepsilon_{Wind}^2 + \varepsilon_{Fit}^2} \quad (A7)$$

757 Here,  $\varepsilon_{TROPOMI}$  is the uncertainty of the NO<sub>2</sub> column concentration,  $\varepsilon_{Wind}$  represents the uncertainty associated with the wind  
758 field, and  $\varepsilon_{Fit}$  accounts for the uncertainty in the fitted vertical scale height and chemical lifetime. The uncertainty of NO<sub>2</sub> arises  
759 from multiple factors, including spectral fitting, stratospheric correction, AMF, clouds, vertical profiles, and surface albedo(Boersma  
760 et al., 2018; Verhoelst et al., 2021; Van Geffen et al., 2022; Lu et al., 2025). In this study, we use the ratio of the standard deviation  
761 to the mean of the column concentration within the study area as a proxy for the TROPOMI observational noise, integrated over the  
762 time series. It should be noted that this proxy is calculated based on the oversampled gridded data (also referred to as Level-3) rather  
763 than the original Level-2 orbit data. In this study, we do not account for errors introduced during the oversampling of TROPOMI  
764 L2 data to the grid(Glissenaar et al., 2025). With appropriate gridding, the uncertainty in polluted areas can be reduced by  
765 approximately 20% compared with the original orbits(Sun et al., 2018a). Wind field uncertainty is quantified through 10<sup>4</sup> Monte  
766 Carlo perturbations of wind speed and direction, with the propagated standard deviation representing the flux variability. The fitting  
767 uncertainty is obtained by performing 10<sup>4</sup> Monte Carlo draws of the grids involved in the fit, generating ensembles of scale heights  
768 and chemical lifetimes, with the final fitting error defined as the root mean square of the standard deviations of these ensembles.

769 Using the method described above, we quantified the overall uncertainty of NO<sub>x</sub> prior emissions for three cities, as well as the  
770 contributions from individual components, with the detailed results summarized in Table A3. It should be noted that the uncertainties  
771 reported here represent aggregated values for the entire urban area, rather than detailed uncertainties for individual grid cells.

772 Based on the uncertainty calculations, the total uncertainty is on the order of ~24% for Beijing, ~18% for Paris, and ~14% for

~~Cairo~~Based on the uncertainty calculations, the total uncertainty follows the order Beijing (23.79%) > Paris (18.15%) > Cairo (14.31%). A closer look at the contributions of individual components reveals that NO<sub>2</sub> column concentrations and the wind field are the dominant sources, together accounting for more than 66.7% of the total uncertainty. This is attributable to the nature of data-driven dispersion models, in which uncertainties in wind and concentration directly govern the overall uncertainty (Sun, 2022). The nonlinear gradient operations in dispersion models (e.g., second-order difference operators) can amplify white noise in the original concentration field, while in existing emission quantification models, wind fields are considered a major source of uncertainty due to sparse monitoring sites and model errors (Huang et al., 2025).

Among the three cities, NO<sub>2</sub> column inversion uncertainty is highest in Beijing. Unlike Cairo, where high surface reflectivity eases retrievals, Beijing is located in the highly polluted North China Plain with elevated AOD, which increases the difficulty of passive column inversion. In addition, Beijing's complex terrain contributes to the highest wind field uncertainty (~17%) among the three cities. The NO<sub>x</sub>/NO<sub>2</sub> uncertainty is roughly similar across the three cities, consistent with previous studies using NU-WRF (~1.4 ± 0.1). In contrast, the uncertainty associated with first-order chemical lifetime and vertical scale height is the lowest among all components (~1%). This is different from earlier studies (~15%) (Liu et al., 2022) and reflects the benefit of the data-driven fitting approach proposed by Sun et al. (see main text). Since no new assumptions were introduced in the current study, this uncertainty arises solely from the linear fitting model.

**Table A3** The overall uncertainty of NO<sub>x</sub> emissions and the uncertainties of individual components were derived using the dispersion model.

	NO <sub>x</sub> /NO <sub>2</sub> uncertainty(%)	NO <sub>2</sub> uncertainty(%)	Wind uncertainty(%)	Fitted uncertainty(%)	Total uncertainty(%)
Beijing	6.51	15.49	16.76	1.67	23.79
Cairo	4.79	11.64	6.76	0.78	14.31
Paris	5.02	13.67	10.76	1.21	18.15

**A6: Optimization results of the CO<sub>2</sub>-to-NO<sub>x</sub> ratio obtained using different calculation methods**

**Table A4** Inversion results of CO<sub>2</sub>-to-NO<sub>x</sub> ratios calculated using different methods

Method	City	Date	Prior CO <sub>2</sub> - to- NO <sub>x</sub>	CO <sub>2</sub> -to- NO <sub>x</sub> ratio uncertainty (%)	NO <sub>x</sub> emission uncertainty (%)	Prior uncertainty (%)	Posterior CO <sub>2</sub> - to-NO <sub>x</sub> ratio (λ)	Posterior uncertainty (%)
--------	------	------	------------------------------------------------------	---------------------------------------------------------------------	------------------------------------------------	-----------------------------	----------------------------------------------------------------	------------------------------

		ratio							
		$(\lambda)$							
1	Beijing	2022/8/9	694	15	23.79	28.12	640	14.08	
	Beijing	2022/8/16	694	15	23.79	28.12	553	16.24	
	Cairo	2022/8/2	470	37.99	14.31	40.60	428	15.09	
	Cairo	2022/8/19	470	37.99	14.31	40.60	512	18.86	
	Paris	2022/8/7	601	24.04	18.15	30.12	731	14.72	
	Paris	2022/8/21	601	24.04	18.15	30.12	742	18.67	
2	Beijing	2022/8/9	632	28.28	23.79	36.96	624	16.08	
	Beijing	2022/8/16	632	28.28	23.79	36.96	521	18.8	
	Cairo	2022/8/2	302	56.56	14.31	58.34	402	23.21	
	Cairo	2022/8/19	302	56.56	14.31	58.34	497	22.14	
	Paris	2022/8/7	412	35.35	18.15	39.74	698	19.65	
	Paris	2022/8/21	412	35.35	18.15	39.74	649	26.14	
3	Beijing	2022/8/9	732	20.02	23.79	31.09	653	17.65	
	Beijing	2022/8/16	732	20.02	23.79	31.09	545	21.32	
	Cairo	2022/8/2	450	45.81	14.31	47.99	412	18.74	
	Cairo	2022/8/19	450	45.08	14.31	47.99	503	20.41	
	Paris	2022/8/7	472	24.83	18.15	30.75	697	16.84	
	Paris	2022/8/21	472	24.83	18.15	30.75	701	19.65	
4	Beijing	2022/8/9	522	26.12	23.79	35.33	594	18.44	
	Beijing	2022/8/16	522	26.12	23.79	35.33	491	15.69	
5	Beijing	2022/8/9	654	18.72	23.79	30.27	630	14.99	
	Beijing	2022/8/16	654	18.72	23.79	30.27	536	20.52	
	Cairo	2022/8/2	420	41.32	14.31	43.73	421	16.79	
	Cairo	2022/8/19	420	41.32	14.31	43.73	532	20.93	
	Paris	2022/8/7	539	28.31	18.15	33.63	720	16.55	
	Paris	2022/8/21	539	28.31	18.15	33.63	718	20.83	
6	Beijing	2022/8/9	610	28.28	23.79	36.96	619	16.55	
	Beijing	2022/8/16	610	28.28	23.79	36.96	509	16.76	

Cairo	2022/8/2	264	56.56	14.31	58.34	403	19.47
Cairo	2022/8/19	264	56.56	14.31	58.34	467	28.12
Paris	2022/8/7	492	35.35	18.15	39.74	687	23.34
Paris	2022/8/21	492	35.35	18.15	39.74	712	23.14

**A7: Posterior fossil fuel emissions distribution for each city**

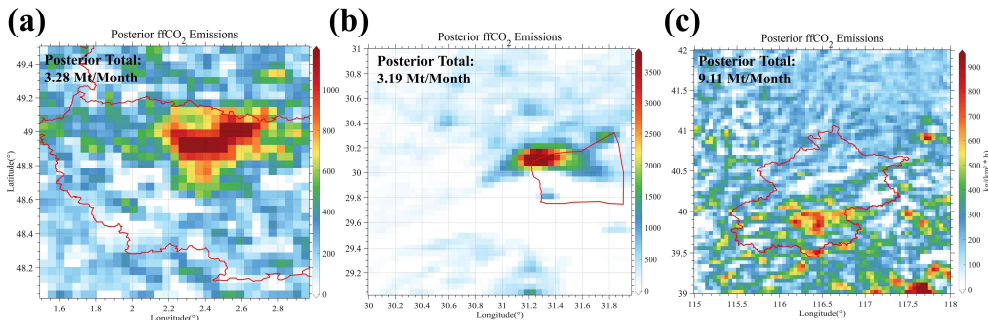


**Figure A1: Posterior fossil fuel carbon dioxide emissions for each city. The red lines outline city boundaries, while the colored shading indicates carbon dioxide emission distribution.**

**Declaration of Competing Interest**

The authors declare that they have no known competing financial interests or personal relationships that could have appeared to influence the work reported in this paper.

**Acknowledgments**

The authors thank all the financial support for this research. This research was supported by the National Key R&D Program of China (Grant No. 2024YFB3910203), National Natural Science Foundation of China(Grant No. 42475144), [the Fundamental Research Funds for the Central Universities\(2042025kf0036\)](#) and Beijing Natural Science Foundation (Grant No. L211045).

**Author contributions**

The experiment design was made by GH and JY. The data collection was done by JY, YH, HL, GH. JY completed the design of the overall WRF-STILT model workflow, data collection, and result analysis. The data analysis was done by HZ, YZ, TS. WG and SL provide funding. The paper was written by JY and GH. All authors have reviewed, commented on, and approved the paper.

808 Reference

809 Agency, I. E.: World energy outlook, OECD/IEA Paris2009.

810 Beirle, S., Borger, C., Jost, A., and Wagner, T.: Improved catalog of NO<sub>x</sub> point source emissions (version 2), *Earth system science*  
811 *data discussions*, 2023, 1-37, 2023.

812 Boersma, K. F., Eskes, H. J., Richter, A., De Smedt, I., Lorente, A., Beirle, S., van Geffen, J. H. G. M., Zara, M., Peters, E., Van  
813 Roozendaal, M., Wagner, T., Maasakkers, J. D., van der A, R. J., Nightingale, J., De Rudder, A., Irie, H., Pinardi, G., Lambert,  
814 J. C., and Compennolle, S. C.: Improving algorithms and uncertainty estimates for satellite NO<sub>2</sub> retrievals: results from the  
815 quality assurance for the essential climate variables (QA4ECV) project, *Atmos. Meas. Tech.*, 11, 6651-6678, 10.5194/amt-11-  
816 6651-2018, 2018.

817 Brenninkmeijer, C. A. and Cai, D. S.: Earth System Chemistry integrated Modelling (ESCiMo) with the Modular Earth Submodel  
818 System (MESSy) version 2.51, *Geoscientific Model Development*, 9, 1153, 2016.

819 Che, K., Lauvaux, T., Taquet, N., Stremme, W., Xu, Y., Alberti, C., Lopez, M., Garcia-Reynoso, A., Ciaia, P., and Liu, Y.: CO<sub>2</sub>  
820 emissions estimate from Mexico City using ground-and space-based remote sensing, *Journal of Geophysical Research:*  
821 *Atmospheres*, 129, e2024JD041297, 2024.

822 Che, K., Cai, Z., Liu, Y., Wu, L., Yang, D., Chen, Y., Meng, X., Zhou, M., Wang, J., Yao, L., and Wang, P.: Lagrangian inversion of  
823 anthropogenic CO<sub>2</sub> emissions from Beijing using differential column measurements, *Environmental Research Letters*, 17,  
824 075001, 10.1088/1748-9326/ac7477, 2022.

825 Cheng, C., Liu, D., Wang, S., Zhang, X., Zhang, L., Chen, W., Liu, J., Wan, X., Chen, W., and Chen, X.: Estimating strong point  
826 CO<sub>2</sub> emissions by combining spaceborne IPDA lidar and HSRL, *Remote Sensing of Environment*, 328, 114898, 2025.

827 Crippa, M., Guizzardi, D., Muntean, M., Schaaf, E., Dentener, F., Van Aardenne, J. A., Monni, S., Doering, U., Olivier, J. G., and  
828 Pagliari, V.: Gridded emissions of air pollutants for the period 1970–2012 within EDGAR v4. 3.2, *Earth Syst. Sci. Data*, 10,  
829 1987-2013, 2018.

830 Dai, G., Wu, S., Long, W., Liu, J., Xie, Y., Sun, K., Meng, F., Song, X., Huang, Z., and Chen, W.: Aerosol and cloud data processing  
831 and optical property retrieval algorithms for the spaceborne ACDL/DQ-1, *Atmospheric Measurement Techniques*, 17, 1879-  
832 1890, 2024.

833 Danielson, J. J. and Gesch, D. B.: Global multi-resolution terrain elevation data 2010 (GMTED2010), US Geological Survey2331-  
834 1258, 2011.

835 Dickerson, R. R., Stedman, D. H., and Delany, A. C.: Direct measurements of ozone and nitrogen dioxide photolysis rates in the  
836 troposphere, *Journal of Geophysical Research: Oceans*, 87, 4933-4946, 1982.

837 Eldering, A., Wennberg, P., Crisp, D., Schimel, D., Gunson, M., Chatterjee, A., Liu, J., Schwandner, F., Sun, Y., and O'dell, C.: The  
838 Orbiting Carbon Observatory-2 early science investigations of regional carbon dioxide fluxes, *Science*, 358, eaam5745, 2017.

839 Eskes, H., van Geffen, J., Sneep, M., Veefkind, P., Niemeijer, S., and Zehner, C.: S5P Nitrogen Dioxide v02. 03.01 intermediate  
840 reprocessing on the S5P-PAL system: Readme file, ESA, 12,

841 Feng, S., Jiang, F., Wang, H., Liu, Y., He, W., Wang, H., Shen, Y., Zhang, L., Jia, M., and Ju, W.: China's fossil fuel CO<sub>2</sub> emissions  
842 estimated using surface observations of coemitted NO<sub>2</sub>, *Environmental Science & Technology*, 58, 8299-8312, 2024.

843 Glissenaar, I., Boersma, K. F., Angloul, I., Rijdsdijk, P., Verhoelst, T., Compennolle, S., Pinardi, G., Lambert, J.-C., Van Roozendaal,  
844 M., and Eskes, H.: TROPOMI Level 3 tropospheric NO<sub>2</sub> dataset with advanced uncertainty analysis from the ESA CCI+ ECV  
845 precursor project, *Earth System Science Data*, 17, 4627-4650, 2025.

846 Hakkarainen, J., Ialongo, I., and Tamminen, J.: Direct space-based observations of anthropogenic CO<sub>2</sub> emission areas from OCO-  
847 2, *Geophysical Research Letters*, 43, 11,400-411,406, 2016.

848 Han, G., Huang, Y., Shi, T., Zhang, H., Li, S., Zhang, H., Chen, W., Liu, J., and Gong, W.: Quantifying CO<sub>2</sub> emissions of power  
849 plants with Aerosols and Carbon Dioxide Lidar onboard DQ-1, *Remote Sensing of Environment*, 313, 114368, 2024.

850 Han, G., Wang, H., Pei, Z., Mao, H., Ying, J., Li, S., Ma, X., Liu, B., Mao, F., and Gong, W.: Quantifying facility-scale CO<sub>2</sub>  
851 emissions using spaceborne hyperspectral imageries, *Remote Sensing of Environment*, 342, 115478, 2026.

852 Han, G., Zhang, H., Huang, Y., Chen, W., Mao, H., Zhang, X., Ma, X., Li, S., Zhang, H., and Liu, J.: First global XCO<sub>2</sub> observations

带格式的: Reference, 缩进: 左侧: 0 厘米, 悬挂缩进: 4 字符

853 fromspaceborne lidar: methodology and initial result, *Remote Sensing of Environment*, 330, 114954, 2025.

854 Hersbach, H., Bell, B., Berrisford, P., Biavati, G., Horányi, A., Muñoz Sabater, J., Nicolas, J., Peubey, C., Radu, R., and Rozum, I.:  
855 ERA5 hourly data on single levels from 1940 to present, Copernicus climate change service (c3s) climate data store (cds), 10,  
856 2023.

857 Huang, T., Zhu, X., Zhong, Q., Yun, X., Meng, W., Li, B., Ma, J., Zeng, E. Y., and Tao, S.: Spatial and temporal trends in global  
858 emissions of nitrogen oxides from 1960 to 2014, *Environmental science & technology*, 51, 7992-8000, 2017.

859 Huang, Y., Han, G., Shi, T., Li, S., Mao, H., Nie, Y., and Gong, W.: Fi-scape: a divergence theorem based emission quantification  
860 model for air/space-borne imaging spectrometer derived xch4 observations, *IEEE Journal of Selected Topics in Applied Earth  
861 Observations and Remote Sensing*, 2024.

862 Huang, Y., Han, G., Yi, J., Shi, T., Zhang, Y., Luo, H., Mao, H., Li, S., Mao, F., and Gong, W.: Rapid methane flux estimation  
863 combining MethaneSAT and Sentinel-5P observations: A case study of Turkmenistan, *Geophysical Research Letters*, 52,  
864 e2025GL119369, 2025.

865 Kiemle, C., Ehret, G., Amediek, A., Fix, A., Quatrevalet, M., and Wirth, M.: Potential of spaceborne lidar measurements of carbon  
866 dioxide and methane emissions from strong point sources, *Remote Sensing*, 9, 1137, 2017.

867 Koene, E. F. M., Brunner, D., and Kuhlmann, G.: On the theory of the divergence method for quantifying source emissions from  
868 satellite observations, *Journal of Geophysical Research: Atmospheres*, 129, e2023JD039904, 2024.

869 Kononov, I. B., Berezin, E. V., Ciaï, P., Broquet, G., Zhuravlev, R. V., and Janssens-Maenhout, G.: Estimation of fossil-fuel CO  
870 2 emissions using satellite measurements of "proxy" species, *Atmospheric Chemistry and Physics*, 16, 13509-13540, 2016.

871 Le Quéré, C., Andrew, R. M., Friedlingstein, P., Sitch, S., Hauck, J., Pongratz, J., Pickers, P. A., Korsbakken, J. I., Peters, G. P., and  
872 Canadell, J. G.: Global carbon budget 2018, *Earth System Science Data*, 10, 2141-2194, 2018.

873 Li, H., Liu, B., Gong, W., Ma, Y., Jin, S., Wang, W., Fan, R., and Jiang, S.: Influence of clouds on planetary boundary layer height:  
874 A comparative study and factors analysis, *Atmospheric Research*, 314, 107784, 2025.

875 Lin, J. and Gerbig, C.: Accounting for the effect of transport errors on tracer inversions, *Geophysical Research Letters*, 32, 2005.

876 Liu, F., Tao, Z., Beirle, S., Joiner, J., Yoshida, Y., Smith, S. J., Knowland, K. E., and Wagner, T.: A new method for inferring city  
877 emissions and lifetimes of nitrogen oxides from high-resolution nitrogen dioxide observations: a model study, *Atmospheric  
878 Chemistry and Physics*, 22, 1333-1349, 2022.

879 Liu, F., Duncan, B. N., Krotkov, N. A., Lamsal, L. N., Beirle, S., Griffin, D., McLinden, C. A., Goldberg, D. L., and Lu, Z.: A  
880 methodology to constrain carbon dioxide emissions from coal-fired power plants using satellite observations of co-emitted  
881 nitrogen dioxide, *Atmospheric Chemistry and Physics*, 20, 99-116, 2020.

882 Liu, M., Van Der A, R., Van Weele, M., Eskes, H., Lu, X., Veeffkind, P., De Laat, J., Kong, H., Wang, J., and Sun, J.: A new divergence  
883 method to quantify methane emissions using observations of Sentinel-5P TROPOMI, *Geophysical Research Letters*, 48,  
884 e2021GL094151, 2021.

885 Lu, L., Cohen, J. B., Qin, K., Tiwari, P., Hu, W., Gao, H., and Zheng, B.: New Perspective on Using Observational Uncertainty to  
886 Improve Reliability of NOx Emissions Over Northern China, *IEEE Transactions on Geoscience and Remote Sensing*, 63, 1-  
887 15, 10.1109/TGRS.2025.3620116, 2025.

888 Luo, B., Yang, J., Shi, S., Gan, R., Wu, Z., Wang, S., Wang, A., Du, L., and Gong, W.: InceptionFormer: A deep learning framework  
889 for UAV LiDAR point cloud completion to improve tree parameters estimation in dense forests, *Remote Sensing of  
890 Environment*, 338, 115348, 2026.

891 Miller, J. B., Tans, P. P., and Gloor, M.: Steps for success of OCO-2, *Nature Geoscience*, 7, 691-691, 2014.

892 Oda, T., Bun, R., Kinakh, V., Topylko, P., Halushchak, M., Marland, G., Lauvaux, T., Jonas, M., Maksyutov, S., and Nahorski, Z.:  
893 Errors and uncertainties in a gridded carbon dioxide emissions inventory, *Mitigation and Adaptation Strategies for Global  
894 Change*, 24, 1007-1050, 2019.

895 Pei, Z., Han, G., Ma, X., Shi, T., and Gong, W.: A method for estimating the background column concentration of CO 2 using the  
896 lagrangian approach, *IEEE Transactions on Geoscience and Remote Sensing*, 60, 1-12, 2022.

897 Qin, K., Lu, L., Liu, J., He, Q., Shi, J., Deng, W., Wang, S., and Cohen, J. B.: Model-free daily inversion of NOx emissions using  
898 TROPOMI (MCMFE-NOx) and its uncertainty: Declining regulated emissions and growth of new sources, *Remote Sensing*

899 of Environment, 295, 113720, 2023.

900 Qu, C., Wang, W., Wu, Z., Wang, L., Liu, K., Wu, L., and Miao, Z.: Zero-Shot Vision-Language Model for Rapid Damaged Bridge  
 901 Extraction in Emergency Response: A Case Study of the 2025 Myanmar Earthquake, *IEEE Geoscience and Remote Sensing*  
 902 *Letters*, 2026.

903 Refaat, T. F., Singh, U. N., Yu, J., Petros, M., Remus, R., and Ismail, S.: Double-pulse 2- $\mu\text{m}$  integrated path differential absorption  
 904 lidar airborne validation for atmospheric carbon dioxide measurement, *Applied Optics*, 55, 4232-4246, 2016.

905 Reuter, M., Buchwitz, M., Schneising, O., Krautwurst, S., O'Dell, C. W., Richter, A., Bovensmann, H., and Burrows, J. P.: Towards  
 906 monitoring localized CO<sub>2</sub> emissions from space: co-located regional CO<sub>2</sub> and NO<sub>2</sub> enhancements observed by the OCO-2  
 907 and SSP satellites, *Atmospheric Chemistry and Physics*, 19, 9371-9383, 2019.

908 Rey-Pommier, A., Chevallier, F., Ciais, P., Christoudias, T., Kushta, J., Georgiou, G., Violaris, A., Dubart, F., and Sciare, J.: Mapping  
 909 NO<sub>x</sub> emissions in Cyprus using TROPOMI observations: evaluation of the flux-divergence scheme using multiple parameter  
 910 sets, *Environmental Science and Pollution Research*, 32, 1932-1951, 2025.

911 Schwandner, F. M., Gunson, M. R., Miller, C. E., Carn, S. A., Eldering, A., Krings, T., Verhulst, K. R., Schimel, D. S., Nguyen, H.  
 912 M., and Crisp, D.: Spaceborne detection of localized carbon dioxide sources, *Science*, 358, eaam5782, 2017.

913 Sheng, M., Hou, Y., Song, H., Ye, X., Lei, L., Ma, P., and Zeng, Z.-C.: Estimating anthropogenic CO<sub>2</sub> emissions from China's  
 914 Yangtze River Delta using OCO-2 observations and WRF-Chem simulations, *Remote Sensing of Environment*, 316, 114515,  
 915 2025.

916 Sun, K.: Derivation of emissions from satellite-observed column amounts and its application to TROPOMI NO<sub>2</sub> and CO  
 917 observations, *Geophysical Research Letters*, 49, e2022GL101102, 2022.

918 Sun, K., Li, L., Jagini, S., and Li, D.: A Satellite Data-Driven Framework to Rapidly Quantify Air Basin-Scale NO<sub>x</sub> Emission and  
 919 Its Application to the Po Valley during the COVID-19 Pandemic, *Atmospheric Chemistry and Physics Discussions*, 2021, 1-  
 920 29, 2021.

921 Sun, K., Zhu, L., Cady-Pereira, K., Chan Miller, C., Chance, K., Clarisse, L., Coheur, P.-F., González Abad, G., Huang, G., and Liu,  
 922 X.: A physics-based approach to oversample multi-satellite, multispecies observations to a common grid, *Atmospheric*  
 923 *Measurement Techniques*, 11, 6679-6701, 2018a.

924 Sun, Y., Frankenberg, C., Jung, M., Joiner, J., Guanter, L., Köhler, P., and Magney, T.: Overview of Solar-Induced chlorophyll  
 925 Fluorescence (SIF) from the Orbiting Carbon Observatory-2: Retrieval, cross-mission comparison, and global monitoring for  
 926 GPP, *Remote sensing of Environment*, 209, 808-823, 2018b.

927 Team, M.: The Multi-resolution Emission Inventory Model for Climate and Air Pollution Research, MEIC Model [data set], 2012.

928 van Geffen, J., Eskes, H., Compernelle, S., Pinardi, G., Verhoelst, T., Lambert, J. C., Sneep, M., ter Linden, M., Ludewig, A.,  
 929 Boersma, K. F., and Veeffkind, J. P.: Sentinel-5P TROPOMI NO<sub>2</sub> retrieval: impact of version v2.2 improvements and  
 930 comparisons with OMI and ground-based data, *Atmos. Meas. Tech.*, 15, 2037-2060, 10.5194/amt-15-2037-2022, 2022.

931 Veeffkind, J. P., Aben, I., McMullan, K., Förster, H., De Vries, J., Otter, G., Claas, J., Eskes, H., De Haan, J., and Kleipool, Q.:  
 932 TROPOMI on the ESA Sentinel-5 Precursor: A GMES mission for global observations of the atmospheric composition for  
 933 climate, air quality and ozone layer applications, *Remote sensing of environment*, 120, 70-83, 2012.

934 Verhoelst, T., Compernelle, S., Pinardi, G., Lambert, J. C., Eskes, H. J., Eichmann, K. U., Fjæraa, A. M., Granville, J., Niemeijer,  
 935 S., Cede, A., Tiefengraber, M., Hendrick, F., Pazmiño, A., Bais, A., Bazureau, A., Boersma, K. F., Bogner, K., Dehn, A., Donner,  
 936 S., Elokhov, A., Gebetsberger, M., Goutail, F., Grutter de la Mora, M., Gruzdev, A., Gratsea, M., Hansen, G. H., Irie, H., Jepsen,  
 937 N., Kanaya, Y., Karagiozidis, D., Kivi, R., Kreher, K., Levelt, P. F., Liu, C., Müller, M., Navarro Comas, M., Piter, A. J. M.,  
 938 Pommereau, J. P., Portafaix, T., Prados-Roman, C., Puenteadura, O., Querel, R., Remmers, J., Richter, A., Rimmer, J., Rivera  
 939 Cárdenas, C., Saavedra de Miguel, L., Sinyakov, V. P., Stremme, W., Strong, K., Van Roozendaal, M., Veeffkind, J. P., Wagner,  
 940 T., Wittrock, F., Yela González, M., and Zehner, C.: Ground-based validation of the Copernicus Sentinel-5P TROPOMI NO<sub>2</sub>  
 941 measurements with the NDACC ZSL-DOAS, MAX-DOAS and Pandonia global networks, *Atmos. Meas. Tech.*, 14, 481-510,  
 942 10.5194/amt-14-481-2021, 2021.

943 Wang, R., Tao, S., Ciais, P., Shen, H., Huang, Y., Chen, H., Shen, G., Wang, B., Li, W., and Zhang, Y.: High-resolution mapping of  
 944 combustion processes and implications for CO<sub>2</sub> emissions, *Atmospheric Chemistry and Physics*, 13, 5189-5203, 2013.

945 Wei, C.: Historical trend and drivers of China's CO<sub>2</sub> emissions from 2000 to 2020, *Environment, development and sustainability*,  
946 26, 2225-2244, 2024.

947 Wu, D., Lin, J. C., Fasoli, B., Oda, T., Ye, X., Lauvaux, T., Yang, E. G., and Kort, E. A.: A Lagrangian approach towards extracting  
948 signals of urban CO<sub>2</sub> emissions from satellite observations of atmospheric column CO<sub>2</sub> (XCO<sub>2</sub>): X-Stochastic Time-Inverted  
949 Lagrangian Transport model ("X-STILT v1"), *Geoscientific Model Development*, 11, 4843-4871, 2018.

950 Xing, Y., Han, G., Mao, H., He, H., Bo, Z., Gong, R., Ma, X., and Gong, W.: MAM-YOLOv9: A Multi-Attention Mechanism  
951 Network for Methane Emission Facility Detection in High-Resolution Satellite Remote Sensing Images, *IEEE Transactions on*  
952 *Geoscience and Remote Sensing*, 2025.

953 Xu, J., Guan, Y., Oldfield, J., Guan, D., and Shan, Y.: China carbon emission accounts 2020-2021, *Applied Energy*, 360, 122837,  
954 2024.

955 Xu, M., Han, G., Pei, Z., Yu, H., Li, S., and Gong, W.: Advanced method for compiling a high-resolution gridded anthropogenic  
956 CO<sub>2</sub> emission inventory at a regional scale, *Geo-spatial Information Science*, 28, 117-130, 2025a.

957 Xu, T., Zhang, C., and Liu, C.: Enhanced quantification of global carbon emitters using collocated OCO-3 CO<sub>2</sub> and NO<sub>2</sub>  
958 observations from twin polar-orbiting satellites, *Geophysical Research Letters*, 52, e2025GL116877, 2025b.

959 Yang, E. G., Kort, E. A., Ott, L. E., Oda, T., and Lin, J. C.: Using space-based CO<sub>2</sub> and NO<sub>2</sub> observations to estimate urban CO<sub>2</sub>  
960 emissions, *Journal of Geophysical Research: Atmospheres*, 128, e2022JD037736, 2023.

961 Ye, X., Lauvaux, T., Kort, E. A., Oda, T., Feng, S., Lin, J. C., Yang, E. G., and Wu, D.: Constraining fossil fuel CO<sub>2</sub> emissions from  
962 urban area using OCO-2 observations of total column CO<sub>2</sub>, *Journal of Geophysical Research: Atmospheres*, 125,  
963 e2019JD030528, 2020.

964 Yi, J., Huang, Y., Pei, Z., and Han, G.: Urban area observing system (UAOS) simulation experiment using DQ-1 total column  
965 concentration observations, *EGU sphere*, 2024, 1-40, 2024.

966 Yi, J., Huang, Y., Pei, Z., and Han, G.: Urban Area Observing System (UAOS) simulation experiment using DQ-1 total column  
967 concentration observations, *Atmospheric Chemistry and Physics*, 25, 13687-13710, 2025.

968 Zhang, H., Han, G., Ma, X., Chen, W., Zhang, X., Liu, J., and Gong, W.: Robust algorithm for precise X CO<sub>2</sub> retrieval using single  
969 observation of IPDA LIDAR, *Optics Express*, 31, 11846-11863, 2023.

970 Zhang, H., Han, G., Chen, W., Pei, Z., Liu, B., Liu, J., Zhang, T., Li, S., and Gong, W.: Validation Method for Spaceborne IPDA  
971 LIDAR  $S_{\{X\}}_{\{C\}\{O\}_2}$  Products via TCCON, *IEEE Journal of Selected Topics*  
972 *in Applied Earth Observations and Remote Sensing*, 17, 16984-16992, 2024.

973 Zhang, Q., Boersma, K. F., Zhao, B., Eskes, H., Chen, C., Zheng, H., and Zhang, X.: Quantifying daily NO<sub>x</sub> and CO<sub>2</sub> emissions  
974 from Wuhan using satellite observations from TROPOMI and OCO-2, *Atmospheric Chemistry and Physics Discussions*, 2022,  
975 1-18, 2022.

976 Zhang, X., Yang, H., Bu, L., Fan, Z., Xiao, W., Chen, B., Zhang, L., Liu, S., Wang, Z., and Liu, J.: Estimation of diurnal emissions  
977 of CO<sub>2</sub> from thermal power plants using spaceborne integrated path differential absorption (IPDA) lidar, *Atmospheric*  
978 *Chemistry and Physics*, 25, 6725-6740, 2025.

979 Zhang, Y., Han, G., Huang, Y., Wang, H., Zhang, H., Pei, Z., Pu, Y., Luo, H., Yi, J., and Shi, T.: Attributing GHG emissions to  
980 individual facilities using multi-temporal hyperspectral images: Methodology and applications, *ISPRS Journal of*  
981 *Photogrammetry and Remote Sensing*, 232, 937-956, 2026.

982 Zheng, B., Geng, G., Ciais, P., Davis, S. J., Martin, R. V., Meng, J., Wu, N., Chevallier, F., Broquet, G., and Boersma, F.: Satellite-  
983 based estimates of decline and rebound in China's CO<sub>2</sub> emissions during COVID-19 pandemic, *Science advances*, 6, eabd4998,  
984 2020.

985